

Quantitative description of strongly correlated materials by combining downfolding techniques and tensor networks

Daan Vrancken,^{1,2} Simon Ganne,¹ Daan Verraes,^{1,2} Tom Braeckvelt,¹
Lukas Devos,² Jutho Haegeman,^{2,*} and Veronique Van Speybroeck^{1,†}

¹*Center for Molecular Modeling, Ghent University, Technologiepark 46, 9052 Zwijnaarde, Belgium*

²*Department of Physics and Astronomy, Ghent University, Krijgslaan 281, 9000 Ghent, Belgium*

(Dated: February 28, 2025)

We present a high-accuracy procedure for electronic structure calculations of strongly correlated materials. The approach involves downfolding the full Hilbert space into a low-energy subspace that captures the most significant electron correlations, leading to an effective Hubbard model. This generalized model is then solved using tensor network methods. Our work focuses on one-dimensional and quasi-one-dimensional materials, for which we employ the machinery of matrix product states. We apply this framework to the conjugated polymers trans-polyacetylene and polythiophene, as well as the quasi-one-dimensional charge-transfer insulator Sr_2CuO_3 . The predicted band gaps exhibit quantitative agreement with state-of-the-art computational techniques and experimental measurements. Beyond band gaps, tensor networks provide access to a wide range of physically relevant properties, including spin magnetization and various excitation energies. Their flexibility supports the implementation of complex Hamiltonians with longer-range interactions, while the bond dimension enables systematic control over accuracy. Furthermore, the computational cost scales efficiently with system size, demonstrating the framework's scalability.

I. INTRODUCTION

Simulating molecules and materials from first principles is essential not only for predicting properties of interest but also for understanding the mechanisms behind emergent phenomena. Techniques like density functional theory (DFT) [1, 2] have enabled the quantitative description of the electronic structure of many materials [3, 4]. The local density approximation (LDA) and generalized gradient approximation (GGA) to the DFT exchange-correlation functional are commonly used to investigate weakly correlated systems. However, the accuracy of these estimations is often insufficient [5, 6], particularly for strongly correlated materials, which exhibit some of the most intriguing and least understood features, such as unconventional superconductivity [7–12], colossal magnetoresistance [13–15], and metal-insulator transitions [16, 17].

Addressing the many-body problem in strongly correlated materials requires more advanced methods [18]. DFT+ U , for example, attempts to compensate for the neglected correlation by introducing an interaction parameter U to the energy functional [19, 20]. Determining the optimal value of U is challenging, often necessitating experimental data, which limits DFT+ U from being a fully first-principles approach. The same issue arises with hybrid functionals [21, 22], where the appropriate mixing of exact exchange and LDA/GGA exchange-correlation can be difficult to predict for strongly correlated materials. Another method is the GW approximation [23, 24], which utilizes many-body perturbation theory and often

provides significant improvements over DFT calculations, particularly for conventional semiconductors and insulators [25]. Yet, even this approach frequently falls short in adequately describing materials with strong electron correlation [26–28]. In wave function-based quantum chemistry, coupled-cluster (CC) techniques [29, 30] and full configuration interaction [31] provide a systematic and precise framework for handling strong correlation, but their high computational cost makes them infeasible for solids.

Alternatively, downfolding methods aim to construct an effective model that captures the essential physics by retaining only the low-energy degrees of freedom [25]. A suitable target space typically includes states that dominate the material's behavior at the low-energy scale. The resulting effective model, often represented as a Hubbard model [32], can then be solved with greater accuracy to extract key physical properties. Although the concept is straightforward, several technical challenges complicate the procedure. One key issue, common to most downfolding routines, is double counting [33]. The screening effects by electrons outside the target space should be incorporated into the two-body interaction parameters, while screening within the low-energy space must be excluded, as it is already accounted for in the effective model. Various constrained methods have been developed to deal with this issue [34–40]. Among them, the constrained random phase approximation (cRPA) [41, 42] is perhaps the most widely used technique for calculating the screened interaction parameters in solids, in part due to its ability to retrieve the frequency-dependence [43]. A second source of double counting arises from the fact that one-body hopping terms are determined from an initial computation that already includes some electron interactions through the Hartree term and the exchange-correlation functional.

* Jutho.Haegeman@UGent.be

† Veronique.VanSpeybroeck@UGent.be

To address this, correction terms can be subtracted from the parameters. Exclusion of the Hartree contribution within the target space is relatively straightforward, but correcting for the exchange-correlation is more difficult. While multiple correction schemes exist [20, 44–46], their impact on the accuracy of simulations remains questionable [33, 47, 48]. On the other hand, a constrained GW (c GW) calculation effectively removes double counting up to the perturbation order within the GW scheme [39].

Once the model is constructed, the next challenge is solving it. Substantial progress has been made with dynamical mean field theory (DMFT) [47, 49, 50], which maps the Hubbard model to an Anderson impurity model [51]. Impurity models can be solved with even greater precision using methods like quantum Monte Carlo (QMC) [52, 53] or coupled-cluster techniques. Conventional DFT+DMFT [20, 47, 54, 55] has been modified to extended DMFT (EDMFT), GW +DMFT, and even GW +EDMFT, offering solutions to some of the initial limitations [56–59]. However, challenges remain, such as the absence of non-local spin fluctuations and non-local vertex corrections beyond RPA [25]. Ongoing research is exploring further extensions to overcome these issues [60–70]. Besides DMFT, other methods like density matrix embedding theory (DMET) [71] and self-energy embedding theory (SEET) [72, 73], which are closely related to DMFT, have been developed, alongside the direct application of solvers such as QMC to the constructed Hubbard model. Directly solving the Hubbard model allows for a more intuitive interpretation as it closely resembles the physical system. Furthermore, the approximations introduced by DMFT and DMET can only be improved by increasing the size of the cluster, leading to exponential growth of the computational cost.

While the applicability of QMC is limited by the sign problem [74], coupled cluster methods are generally impractical for realistic multi-band Hubbard models beyond the singles and doubles (CCSD) approximation. In the past two decades, tensor networks (TNs) [75] have emerged as powerful tools for describing interacting quantum lattice systems. They are applicable to generalized Hubbard models with longer-range interactions while maintaining a computational cost that scales favorably with system size according to the area law of entanglement [75, 76]. Additionally, the bond dimension is a tunable parameter for simulation accuracy, with infinite bond dimension representing the exact solution, though convergence is often achievable with relatively small, feasible values. Serious attention was first drawn to TNs after the success of the density matrix renormalization group (DMRG) [77] algorithm, now well established [78]. DMRG efficiently optimizes matrix product states (MPS) [79–81], a one-dimensional TN Ansatz. Algorithms based on projected entangled-pair states (PEPS) [76, 82] show increasing promise for higher-dimensional systems, particularly for fermionic systems where the sign problem excludes QMC. However, these higher-dimensional TN methods remain relatively new compared to many other

techniques, and intensive research continues to broaden their performance and applicability.

In this work, we use DFT+cRPA to construct an effective multi-band Hubbard model for several one-dimensional (1D) and quasi-1D materials, which we then solve using MPS methods. Conjugated polymers provide ideal benchmark systems for our approach [83]. These organic semiconductors were extensively investigated during the late 20th century [84–89], leading to the Nobel Prize in Chemistry in 2000 for the discovery and development of conductive polymers. With their continued relevance in modern applications such as flexible electronics, biosensors, and light-emitting diodes [83, 90], conjugated polymers remain of significant interest. The band gap, obtainable via TN calculations, will be an important quantity to validate the procedure. Although optical and band gap measurements are often limited to bulk samples, angle-resolved photoemission spectroscopy (ARPES) experiments on individual chains have recently been demonstrated [91]. Specifically, we will study trans-polyacetylene (tPA) and polythiophene (PT), due to their extensive presence in the literature. Their crystal structures are shown in Fig. 1a and b.

In addition to purely 1D materials, we examine the quasi-1D system Sr_2CuO_3 . As illustrated in Fig. 1c, infinite chains of corner-sharing CuO_4 squares are embedded within its three-dimensional crystal structure [92]. These chains are well-isolated, allowing the low-energy physics to be effectively treated as one-dimensional. Sr_2CuO_3 may allow insights in the mechanisms behind superconducting cuprates through oxygen doping [93]. It also provides a rich platform for exploring spin-charge separation, where single-particle excitations split into spinons and holons carrying spin and charge, respectively [94, 95], as observed in ARPES experiments [96, 97]. Its antiferromagnetic spin structure along the chain and the elementary excitations are observables that are accessible through TN calculations of the Hubbard model.

The purpose of this paper is twofold. First, we demonstrate the effectiveness of tensor networks in modeling real materials. Although our focus is on one-dimensional systems, the transition to higher-dimensional PEPS calculations, anticipated in the near future, is expected to follow a similar framework. Second, we introduce a novel ab initio simulation technique for strongly correlated electron systems, applicable to both purely 1D materials and those exhibiting a strong one-dimensional character. This approach not only captures electron correlation accurately through effective models with a high number of bands and longer-range interactions, but also provides access to various excitations. Additionally, the bond dimension offers systematic control over accuracy, with computational costs scaling efficiently as system size increases. The next section outlines our approach. Section III presents the results, while we draw our conclusions in Section IV. Finally, Section V elaborates on the computational details.

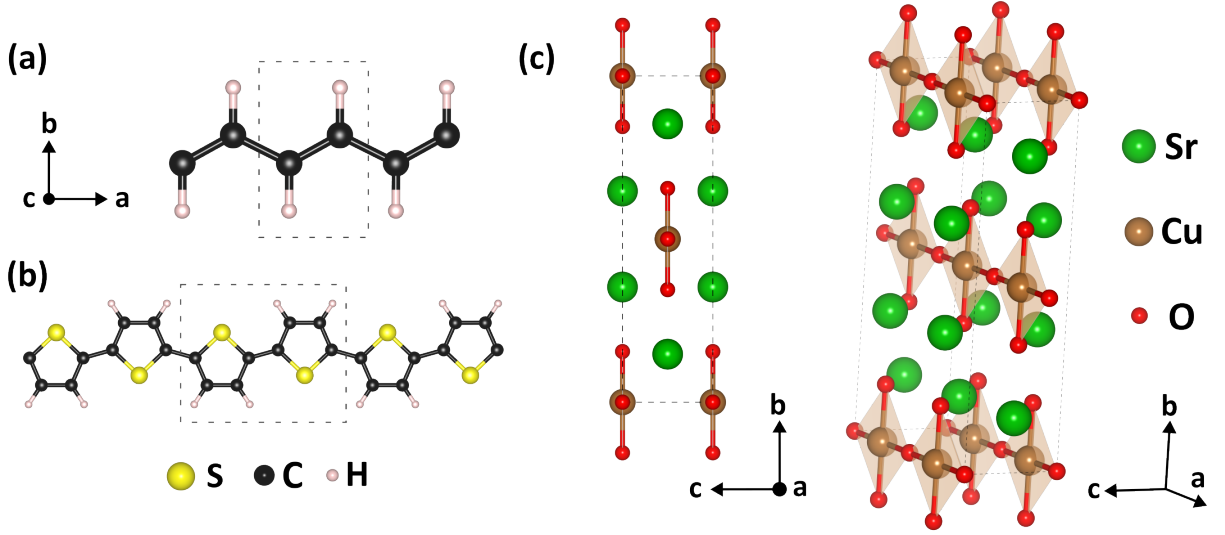


FIG. 1. Crystal structures of (a) trans-polyacetylene, (b) polythiophene, and (c) Sr_2CuO_3 in two perspectives. The dashed lines indicate the unit cells.

II. METHODOLOGY

The central problem of the current work is the many-body problem, and more specifically, the electronic structure of strongly correlated materials. The proposed procedure consists of two main components: constructing the Hubbard model and solving it. Fig. 2 illustrates the various steps of our method. We begin by explaining the theory behind the downfolding algorithm, followed by a description of how tensor networks are applied to solve the low-energy model.

A. Downfolding

We consider a generalized 1D multi-band Hubbard model with Hamiltonian of the form

$$H = - \sum_{i,j} \sum_{\alpha,\beta} \sum_{\sigma} t_{ij}^{\alpha\beta} c_{i\alpha\sigma}^\dagger c_{j\beta\sigma} + \frac{1}{2} \sum_{i,j,k,l} \sum_{\alpha,\beta,\gamma,\delta} \sum_{\sigma,\sigma'} U_{ijkl}^{\alpha\beta\gamma\delta} c_{i\alpha\sigma}^\dagger c_{k\gamma\sigma'}^\dagger c_{l\delta\sigma'} c_{j\beta\sigma}. \quad (1)$$

Here, σ and σ' label the spin state of the electron, the Latin indices i, j, k, l label the sites in the lattice, and the Greek indices $\alpha, \beta, \gamma, \delta$ the different orbitals on a site. $t_{ij}^{\alpha\beta}$ gives the hopping strength from orbital α on site i to orbital β on site j , while $U_{ijkl}^{\alpha\beta\gamma\delta}$ are the Coulomb integrals. Finally, $c_{i\alpha\sigma}^\dagger$ ($c_{i\alpha\sigma}$) is the creation (annihilation) operator of an electron with spin σ in orbital α on site i . A generalization to spin-dependent parameters can be made by including the spin in the orbital index $\alpha \rightarrow \bar{\alpha} = (\alpha, \sigma)$, resulting in twice as many orbitals, which can only be occupied by a single electron.

The goal is to determine the parameters $t_{ij}^{\alpha\beta}$ and $U_{ijkl}^{\alpha\beta\gamma\delta}$ such that the model accurately represents the low-energy subspace of the considered material. The process begins with an initial DFT simulation, from which a suitable target space is identified using maximally localized Wannier functions (MLWFs) [98]. Next, cRPA is used to calculate the Coulomb integrals. Lastly, corrections are made to account for the double counting of interactions in the hopping parameters.

1. DFT and target space

The starting point of the procedure is an initial DFT calculation of the material. With a relatively cheap exchange-correlation functional, like the Perdew-Burke-Ernzerhof (PBE)-GGA [99], the Kohn-Sham orbitals and corresponding eigenvalues can be calculated, leading to an approximate band structure. Assuming that DFT provides sufficient accuracy when correlations are weak, a subset of bands should be chosen to define the low-energy space where strong correlation effects are incorporated in the effective model. In order to keep the computational cost low, this target space is preferably as small as possible without neglecting relevant physics. Typically, correlations are expected to be strong in narrow and partially occupied bands close to the Fermi energy. For bands further away from the Fermi energy, it is assumed that correlations are weak and, consequently, that DFT is accurate.

Once an appropriate low-energy space is chosen, an MLWF basis set is constructed from the included bands. The Wannier functions are of the form [100]

$$\phi_{\alpha\mathbf{R}}(\mathbf{r}) = \frac{V}{(2\pi)^3} \int e^{-i\mathbf{k}\cdot\mathbf{R}} \tilde{\psi}_{\alpha\mathbf{k}}(\mathbf{r}) d\mathbf{k}, \quad (2)$$

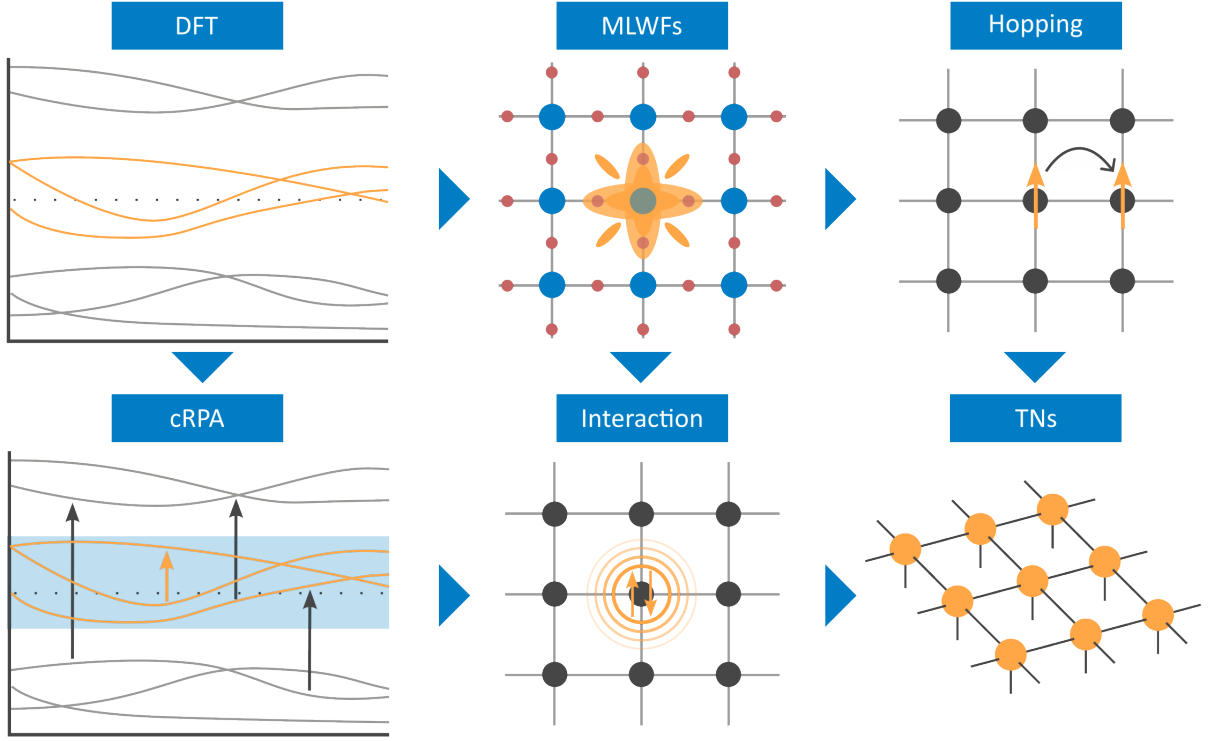


FIG. 2. Schematic representation of the various steps in the downfolding procedure. Top left to top right: First, a DFT calculation is performed on the material. A set of bands is then chosen as target space and is used to construct MLWFs. Calculating the matrix elements of the Kohn-Sham Hamiltonian in the MLWF basis yields the tight-binding parameters of the Hubbard model. Double counting is then eliminated. Bottom left to bottom right: cRPA is carried out on the selected low-energy subspace, with a disentanglement method applied when required. The interaction matrix elements are computed by evaluating the partially screened Coulomb interaction in the MLWF basis. Finally, the hopping and interaction parameters define a Hubbard model which is implemented and solved with tensor network algorithms.

where the integral is over the first Brillouin zone, V is the real-space primitive cell volume, \mathbf{R} is a real-space lattice vector, and

$$\tilde{\psi}_{\alpha\mathbf{k}}(\mathbf{r}) = \sum_{\beta} T_{\alpha\beta}^{(\mathbf{k})} \psi_{\beta\mathbf{k}}(\mathbf{r}) \quad (3)$$

is a linear combination of Bloch functions $\psi_{\beta\mathbf{k}}(\mathbf{r})$, which can be approximated by the Kohn-Sham orbitals. For a spin-polarized DFT calculation, the spin is included in the orbital index. When the Brillouin zone is discretized into a set of N_k k -points, as is the case in DFT calculations, Equation (2) becomes

$$\phi_{\alpha\mathbf{R}}(\mathbf{r}) = \frac{1}{N_k} \sum_{\beta\mathbf{k}} e^{-i\mathbf{k}\cdot\mathbf{R}} T_{\alpha\beta}^{(\mathbf{k})} \psi_{\beta\mathbf{k}}(\mathbf{r}). \quad (4)$$

The expansion coefficients, $T_{\alpha\beta}^{(\mathbf{k})}$, are uniquely defined by imposing that the spread

$$\Omega = \sum_{\alpha} \left(\langle \phi_{\alpha\mathbf{0}} | r^2 | \phi_{\alpha\mathbf{0}} \rangle - \langle \phi_{\alpha\mathbf{0}} | \mathbf{r} | \phi_{\alpha\mathbf{0}} \rangle^2 \right), \quad (5)$$

is minimized, resulting in Wannier functions that are maximally localized in real space. The goal of using MLWFs is to localize interactions in the Hubbard model,

minimizing the challenges of dealing with long-range effects.

2. Coulomb integrals

When a suitable low-energy space with corresponding MLWFs is obtained, the parameters defining the Hubbard model can be computed. In many-body perturbation theory, the screened interaction is given by

$$W = \frac{v}{1 - vP} \quad (6)$$

as a function of the bare interaction $v(\mathbf{r}, \mathbf{r}') = 1/|\mathbf{r} - \mathbf{r}'|$. Within the random phase approximation, the polarization function P is related to the Green's function as

$$P = -iGG \quad (7)$$

in shorthand notation. Additionally, P is identified with the response function of a non-interacting system [25]. In the frequency domain, the non-interacting Green's func-

tion takes the form

$$G_0(\mathbf{r}, \mathbf{r}', \omega) = \sum_{\alpha\mathbf{k}}^{\text{occ}} \frac{\psi_{\alpha\mathbf{k}}(\mathbf{r})\psi_{\alpha\mathbf{k}}^*(\mathbf{r}')}{\omega - \varepsilon_{\alpha\mathbf{k}} - i\eta} + \sum_{\alpha\mathbf{k}}^{\text{unocc}} \frac{\psi_{\alpha\mathbf{k}}(\mathbf{r})\psi_{\alpha\mathbf{k}}^*(\mathbf{r}')}{\omega - \varepsilon_{\alpha\mathbf{k}} + i\eta} \quad (8)$$

so that

$$P(\mathbf{r}, \mathbf{r}', \omega) = -i \int \frac{d\omega'}{2\pi} G_0(\mathbf{r}, \mathbf{r}', \omega + \omega') G_0(\mathbf{r}, \mathbf{r}', \omega') \\ = \sum_{\alpha\mathbf{k}}^{\text{occ}} \sum_{\alpha'\mathbf{k}'}^{\text{unocc}} \left[\frac{\psi_{\alpha\mathbf{k}}^*(\mathbf{r})\psi_{\alpha'\mathbf{k}'}(\mathbf{r})\psi_{\alpha'\mathbf{k}'}^*(\mathbf{r}')\psi_{\alpha\mathbf{k}}(\mathbf{r}')}{\omega - \varepsilon_{\alpha'\mathbf{k}'} + \varepsilon_{\alpha\mathbf{k}} + i\eta} - \frac{\psi_{\alpha\mathbf{k}}(\mathbf{r})\psi_{\alpha'\mathbf{k}'}^*(\mathbf{r})\psi_{\alpha'\mathbf{k}'}(\mathbf{r}')\psi_{\alpha\mathbf{k}}^*(\mathbf{r}')}{\omega + \varepsilon_{\alpha'\mathbf{k}'} - \varepsilon_{\alpha\mathbf{k}} - i\eta} \right], \quad (9)$$

with $\varepsilon_{\alpha\mathbf{k}}$ the eigenvalue corresponding to orbital $\psi_{\alpha\mathbf{k}}(\mathbf{r})$ and η an infinitesimally small positive number [101]. The summations over the occupied and unoccupied states can be interpreted as a summation over all possible transitions from below the Fermi energy to above.

The main idea of the cRPA is then to split this sum into the transitions within the chosen low-energy subspace and the remaining transitions, $P = P_l + P_r$. As the screening due to states within the target space is included in the effective model, we exclude them from the screened interaction to arrive at a partially screened interaction,

$$W_r = \frac{v}{1 - vP_r}, \quad (10)$$

which is to be encoded in the Hubbard U parameters. However, separating the sum into P_l and P_r is not trivial when the bands of the two subspaces are entangled with each other. Several techniques, such as the disentanglement [102], weighted [103], and projector [104] methods, have been developed to overcome this issue. In this work, the projector method has been used.

The matrix elements of U in the basis spanned by the MLWFs are

$$U_{ijkl}^{\alpha\beta\gamma\delta}(\omega) = \int \int d\mathbf{r} d\mathbf{r}' \phi_{\alpha\mathbf{R}_i}^*(\mathbf{r}) \phi_{\beta\mathbf{R}_j}(\mathbf{r}) \\ W_r(\mathbf{r}, \mathbf{r}', \omega) \phi_{\gamma\mathbf{R}_k}^*(\mathbf{r}') \phi_{\delta\mathbf{R}_l}(\mathbf{r}'). \quad (11)$$

In 1D systems, the lattice vectors relate to the site indices as $\mathbf{R}_i = [i, 0, 0]$.

Although frequency dependence can have non-negligible effects [39, 105, 106], the static limit approximation is employed by setting $\omega = 0$. Dynamical features, which reduce the over- or under-screening of static parameters, will be considered in future work.

3. Hopping parameters

In a first approximation, the hopping parameters can be calculated as

$$\tilde{t}_{ij}^{\alpha\beta} = -\langle \phi_{\alpha\mathbf{R}_i} | H^{KS} | \phi_{\beta\mathbf{R}_j} \rangle \\ = -\int d\mathbf{r} \phi_{\alpha\mathbf{R}_i}^*(\mathbf{r}) H^{KS} \phi_{\beta\mathbf{R}_j}(\mathbf{r}), \quad (12)$$

with H^{KS} the Kohn-Sham Hamiltonian. However, the Hartree term V^h and exchange-correlation energy V^{xc} should be constrained to exclude the interactions within the target space. The low-energy Hartree contribution to parameter $t_{ij}^{\alpha\beta}$ is given by [45, 107, 108]

$$t_{ij}^{(h)\alpha\beta} = -\langle \phi_{\alpha\mathbf{R}_i} | V_{\text{eff}}^h | \phi_{\beta\mathbf{R}_j} \rangle \\ = -\sum_{k,l} \sum_{\gamma,\delta} \rho_{k,l}^{\gamma\delta} U_{ijkl}^{\alpha\beta\gamma\delta}, \quad (13)$$

with V_{eff}^h the partially screened Hartree term and $\rho_{k,l}^{\alpha,\beta}$ the single-particle occupation matrix in the MLWF basis, obtained from DFT. One can choose to sum only over the interaction parameters included in the effective model, treating the remaining interactions in a mean-field way, or to sum over all $U_{ijkl}^{\alpha\beta\gamma\delta}$. In the latter case, the sum is truncated for large k and l , since the interaction parameters decay with distance. We employ this approach, exclusively incorporating interactions into the two-body terms.

The exchange-correlation functional, on the other hand, is difficult to separate into high- and low-energy contributions, but in the GW approximation, the self-energy can be written as [39]

$$\Sigma = iGW = iG_l W + iG_r W. \quad (14)$$

The Green's function G has been split into a low-energy part G_l and the rest G_r , which is equivalent to the high-energy part. If we then subtract V^{xc} from the Kohn-Sham Hamiltonian and add the constrained self-energy $\Sigma_r = iG_r W$, the self-energy of the low-energy space is neglected

$$t_{ij}^{\alpha\beta} = -\langle \phi_{\alpha\mathbf{R}_i} | H^{KS} - V_{\text{eff}}^h - V^{xc} + \Sigma_r | \phi_{\beta\mathbf{R}_j} \rangle \\ = \tilde{t}_{ij}^{\alpha\beta} - t_{ij}^{(h)\alpha\beta} + \langle \phi_{\alpha\mathbf{R}_i} | V^{xc} - \Sigma_r | \phi_{\beta\mathbf{R}_j} \rangle. \quad (15)$$

This constrained GW approach effectively eliminates the double-counting error in the one-body terms.

While the calculation of the Hartree correction term is relatively straightforward, the implementation and benchmarking of the cGW approach are significantly more challenging. Exchange-correlation double counting is typically considered less critical [20] and is therefore disregarded, leaving cGW as the primary focus for ongoing and future work.

B. Solving the Hubbard model

Once the parameters of the Hubbard model have been determined, the properties of interest can be computed. In the following, we briefly introduce the concept of matrix product states and the algorithms used to find the ground and excited states.

1. Matrix product states

Any quantum state of a lattice model with N sites can be expressed as an expansion over basis states,

$$|\psi\rangle = \sum_{s_1, \dots, s_N} C_{s_1, \dots, s_N} |s_1, \dots, s_N\rangle \in (\mathbb{C}^d)^{\otimes N}, \quad (16)$$

and is uniquely defined by the coefficients C_{s_1, \dots, s_N} . The sum spans the physical Hilbert space at each site. In the single-band Hubbard model, for instance, the local Hilbert space is four-dimensional ($d = 4$), with the basis $\{|0\rangle, |\uparrow\rangle, |\downarrow\rangle, |\uparrow\downarrow\rangle\}$, where arrows denote the electron spins. By repeatedly applying a singular value decomposition (SVD), we can rewrite the tensor C as [109]

$$|\psi\rangle = \sum_{s_1, \dots, s_N} A_{s_1}^{(1)} \dots A_{s_N}^{(N)} |s_1, \dots, s_N\rangle \quad (17)$$

with $A_{s_i}^{(i)}$ a $D_i \times D_{i+1}$ matrix and $D_1 = D_{N+1} = 1$, hence the name MPS. The bond dimension D_i indicates the number of leading singular values retained in the SVD. Any state can be written in this form on the condition that the bond dimensions are sufficiently large [110]. In practice, finite values of $D = \max_i \{D_i\}$ are used to approximate the state and keep the simulations feasible.

In the thermodynamic limit, a uniform MPS takes the

form [111]

$$|\psi\rangle = \sum_{\{s\}} \mathbf{v}_L^\dagger \left(\prod_{m \in \mathbb{Z}} A_{s_m} \right) \mathbf{v}_R |\{s\}\rangle \\ = \dots \text{---} \boxed{A} \text{---} \boxed{A} \text{---} \boxed{A} \text{---} \dots \quad (18)$$

The column vectors \mathbf{v}_L and \mathbf{v}_R handle the boundary conditions, but carry no physical meaning as we work in an infinite system. In Equation (18), we introduced the diagrammatic notation for tensor networks. Shapes represent tensors and legs their indices. Here, the legs pointing downward correspond to the physical Hilbert space of dimension d , while the horizontal legs denote the virtual spaces of dimension D . Connected legs imply contraction of the indices. Generally, the unit cell can be expanded to multiple sites, forming a similar chain but with different repeating tensors.

2. Ground state

To compute the ground state, we look for the state that minimizes the energy. In the one-site DMRG variant, all matrices A are fixed except one, which is optimized. The algorithm then moves to the next matrix, iteratively sweeping back and forth along the chain until convergence. The improved two-site DMRG variant, combines two matrices into a single block, optimizes it, and then splits it back into two sites via SVD, enabling dynamic control of the bond dimension. For a detailed discussion on DMRG, including applications to infinite systems, see review articles [78, 112, 113].

Another MPS optimization method is the variational uniform matrix product states (VUMPS) algorithm [114], based on tangent-space techniques. VUMPS typically converges faster than infinite DMRG in systems with longer-range interactions. Both algorithms are employed in this work.

3. Quasiparticle excitations

In addition to the system's ground state, we are interested in elementary excitations, which enable the calculation of the band gap. The quasiparticle Ansatz in the context of MPS, as introduced by Haegeman et al. [115, 116], is given by the expression

$$|\psi_k(B)\rangle = \sum_n e^{ikn} \sum_{\{s\}} \mathbf{v}_L^\dagger \left(\prod_{m < n} A_{s_m} \right) B_{s_n} \left(\prod_{m > n} A_{s_m} \right) \mathbf{v}_R |\{s\}\rangle \\ = \sum_n e^{ikn} (\dots \text{---} \boxed{A} \text{---} \boxed{A} \text{---} \boxed{B} \text{---} \boxed{A} \text{---} \boxed{A} \text{---} \dots) \quad (19)$$

$\vdots \qquad \qquad \qquad s_{n-1} \qquad \qquad s_n \qquad \qquad s_{n+1} \qquad \qquad \vdots$

In this approach, one tensor A of the ground state is modified, introducing a perturbation localized around site n , followed by a momentum superposition. The elements of the newly introduced tensor B act as variational parameters.

For this Ansatz, the minimization of the energy functional

$$\min_B \frac{\langle \psi_k(B) | H | \psi_k(B) \rangle}{\langle \psi_k(B) | \psi_k(B) \rangle} \quad (20)$$

reduces to the generalized eigenvalue problem

$$H_{\text{eff}}(k)\mathbf{B} = \omega N_{\text{eff}}(k)\mathbf{B} \quad (21)$$

with \mathbf{B} a vectorized version of the matrix B . The effective Hamiltonian H_{eff} and normalization matrix N_{eff} are defined by the relations

$$2\pi\delta(k - k')(\mathbf{B}')^\dagger H_{\text{eff}}(k)\mathbf{B} = \langle \psi_{k'}(B') | H | \psi_k(B) \rangle \quad (22)$$

$$2\pi\delta(k - k')(\mathbf{B}')^\dagger N_{\text{eff}}(k)\mathbf{B} = \langle \psi_{k'}(B') | \psi_k(B) \rangle, \quad (23)$$

where the δ functions follow from the translation invariance of H . Furthermore, it is possible to parameterize B in terms of new parameters with respect to which N_{eff} becomes the identity matrix, thereby simplifying the problem to an ordinary eigenvalue problem. As H_{eff} is Hermitian, the iterative Lanczos algorithm can efficiently compute the lowest eigenvalues and eigenvectors with a computational complexity of $\mathcal{O}(D^3)$ [111].

This variational approach approximates the stationary eigenstates of the fully interacting Hamiltonian, yielding quasiparticles with infinite lifetimes, unlike standard perturbative methods. While it is formally guaranteed to work for gapped systems, it also delivers excellent results for gapless systems. A potential limitation arises for large physical operators, as the Ansatz may struggle to represent wide excitations, even with increasing bond dimension. Expanding B -blocks offers a solution, but at the cost of an exponential increase in the number of variational parameters.

Despite this, the quasiparticle Ansatz is highly suitable for our purposes, particularly in identifying the lowest-lying single-particle excitations. For applications to uniform MPS with larger unit cells, we refer to the work of Zauner-Stauber et al. [117].

III. RESULTS AND DISCUSSION

We present the results of our approach applied to tPA, PT, and Sr_2CuO_3 . For tPA, a relatively simple system, we focus on the flexibility and quantitative accuracy that is offered by TNs. In the case of PT, we demonstrate the feasibility of effective models containing a large number of bands. Finally, we show that our approach is also applicable to quasi-1D materials such as Sr_2CuO_3 . More information on the computational details can be found in Section V.

A. Trans-polyacetylene

Polyacetylene is the simplest conjugated polymer, existing in two configurations: trans- (see Fig. 1a) and cis-polyacetylene. The cis isomer is thermodynamically less stable and converts to the trans form upon heating, allowing the preparation of pure trans samples for experimental studies [118]. Therefore, our discussion focuses on trans-polyacetylene.

The primitive unit cell contains two carbon and two hydrogen atoms. It is widely accepted that alternating single and double carbon-carbon bonds occur along the chain, leading to a band gap due to Peierls instability [119]. However, the presence of this dimerization remains debated [120]. The band gap is highly sensitive to the degree of bond length alternation (BLA), but experimentally determining this alternation is challenging. Moreover, our geometry optimization shows that the BLA depends strongly on computational settings, including the choice of DFT functional, basis set, and even the parity of the k -grid.

To address this, we analyze three geometries with varying BLA values. These structures, labeled tPA1, tPA2, and tPA3, have unit cell widths along the chain of $a = 2.471$ Å, 2.457 Å, and 2.449 Å, respectively. Their BLA values are 1.396 Å / 1.396 Å (no alternation up to three decimal places), 1.374 Å / 1.403 Å, and 1.360 Å / 1.434 Å. The geometry with the largest alternation (tPA3) was taken from other recent studies [121–123], facilitating comparison of results.

1. Downfolding

The first step in this approach is the DFT simulation. Fig. 3 presents the band structure for the three tPA geometries. The valence and conduction bands, predominantly of carbon p_z character, are separated by a small band gap. As expected, the gap increases with a larger BLA, however, even for tPA3, its value remains significantly underestimated. From these bands, two MLWFs are constructed, each centered on a carbon atom within the unit cell. Consequently, the effective model corresponds to a two-band Hubbard model at half-filling.

The hopping parameters $t_{ij}^{\alpha\beta}$, obtained via Hartree correction of the tight-binding parameters, and the direct Coulomb interaction $U_{ij}^{\alpha\beta} = U_{iijj}^{\alpha\alpha\beta\beta}$ from cRPA are presented in Table I for tPA3. The remaining parameters, as well as those for the other two structures, are provided in Appendix C. By subtracting a constant chemical potential, the diagonal terms of the on-site hopping matrix are adjusted to set the smallest value on the diagonal to zero.

The decreasing values for increasing distances suggest that the Wannier functions are well-localized, although $U_{ij}^{\alpha\beta}$ retains significant magnitude even over extended ranges. Notably, the dominant one-body param-

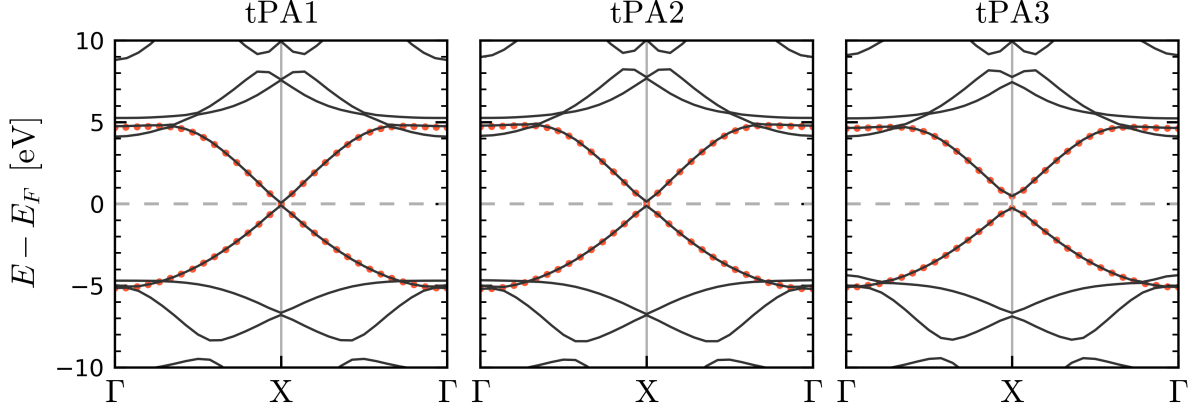


FIG. 3. The electronic band structure of trans-polyacetylene geometries tPA1, tPA2, and tPA3, with the Fermi energy E_F shifted to 0 eV. The dotted lines are the Wannier interpolated bands. The high-symmetry points of the Brillouin zone are labeled by $\Gamma = (0, 0, 0)$ and $X = (0.5, 0, 0)$.

TABLE I. Hopping matrices $t_{ij}^{\alpha\beta}$ from tight-binding approximation with Hartree correction and direct Coulomb interaction $U_{ij}^{\alpha\beta}$ from cRPA for tPA3. The elements (in eV) correspond to the hopping/interaction parameter between band α on site $\mathbf{R}_i = [0, 0, 0]$ (rows) and band β on different sites $\mathbf{R}_j = [j, 0, 0]$ (columns).

t							
[0,0,0]	[1,0,0]	[2,0,0]	[3,0,0]				
0.000	3.803	-0.548	0.298	-0.010	-0.034	0.031	-0.024
3.803	0.000	2.977	-0.501	0.005	-0.010	-0.022	0.029
U							
[0,0,0]	[1,0,0]	[2,0,0]	[3,0,0]				
10.317	6.264	4.407	3.075	2.284	1.719	1.319	1.011
6.264	10.317	6.162	4.407	3.065	2.284	1.710	1.319

eters occur between neighboring carbon atoms. The distinction between single and double bonds aligns with the well-known Su-Schrieffer-Heeger model for trans-polyacetylene [124]. Compared to the other geometries, the primary difference lies in the ratio t_{00}^{12}/t_{01}^{21} , while the interactions remain largely unchanged. Terms on the same diagonal of the $U_{ij}^{\alpha\beta}$ matrix are approximately equal in magnitude, as they represent interactions over the same physical distance in the lattice.

For each geometry, we analyze multiple models. The hopping range is selected to include all terms listed in Table I except the parameter above the diagonal of the $[3, 0, 0]$ matrix, t_{03}^{12} , ensuring consistency with the corresponding physical distances. Regarding interactions, we incorporate all terms up to a specified range R . For $R = 1$, only interactions between neighboring orbitals are included; for $R = 2$, next-to-nearest neighbor interactions are added, and so on. We extend this up to $R = 4$, which includes all direct interactions larger than

2 eV in Table I, for example. As previously noted, all interaction terms within this range are considered, encompassing not only the direct interactions $U_{ij}^{\alpha\beta}$ but also the exchange terms $J_{ij}^{\alpha\beta} = U_{ijij}^{\alpha\beta\alpha\beta} = U_{ijji}^{\alpha\beta\beta\alpha}$, those of the form $\tilde{U}_{ij}^{\alpha\beta} \equiv U_{ijjj}^{\alpha\beta\beta\beta}$, and even interactions involving three or four different orbitals, such as $U_{ijkk}^{\alpha\beta\gamma\gamma}$ and $U_{ijkl}^{\alpha\beta\gamma\delta}$. Parameters smaller than 10 meV are excluded.

2. Model solution

The models defined above are implemented and solved using tensor network code, as described in Section V. With the quasiparticle Ansatz, the first single-particle and single-hole excitation energies, $E_+[k]$ and $E_-[k]$ respectively, are calculated for momenta $k \in [0.0, \pi/4, 2\pi/4, 3\pi/4, \pi]$ along the chain. The minimum of the sum of these excitations determines the band gap of the system

$$E_g = \min_k (E_+[k] + E_-[k] - 2E_0), \quad (24)$$

where E_0 is the ground state energy. For all tPA geometries, we always find the minimum at momentum $k = 0.0$.

Fig. 4 illustrates the band gap for different geometries as a function of the range R . The dashed line represents the experimental value reported by Wang et al. [91], obtained via scanning tunneling spectroscopy and differential conductance spectroscopy on single tPA chains. The dotted line marks the value computed using equation-of-motion CCSD (EOM-CCSD), extrapolated to the thermodynamic limit by Moerman et al. [123].

The band gap predicted by the $R = 1$ models deviates significantly from the other results, highlighting the importance of longer-range interactions. For tPA1, the geometry with the smallest gap, a value of 2.09 eV is obtained, whereas tPA2 has a gap of 3.15 eV. This

suggests that the geometry studied in Wang et al.'s experiment has a smaller BLA than typically assumed for tPA. In contrast, tPA3 exhibits a much larger gap of 4.28 eV, closer to the coupled-cluster prediction. The remaining discrepancy may arise from finite-size effects in the EOM-CCSD extrapolation to the thermodynamic limit, the restriction to singles and doubles excitations, or the absence of *cGW* and frequency corrections in the present approach.

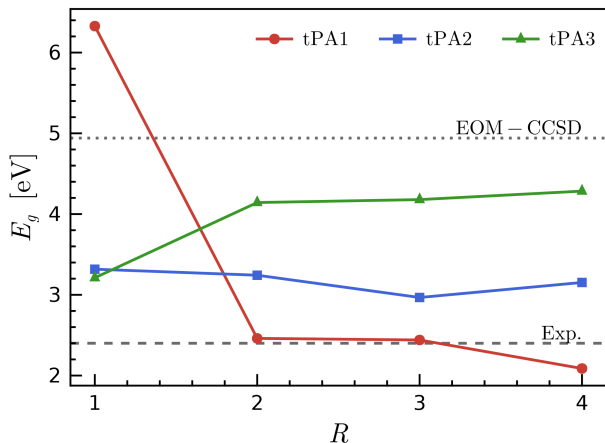


FIG. 4. Band gap of three different geometries of tPA as a function of the maximal interaction range R . The dashed line indicates the experimental value found in [91], while the dotted line is the value obtained with EOM-CCSD for tPA3 in [123].

Table II compares the band gaps predicted by our method (DFT+TN) with those obtained using other computational methods performed with VASP. Regardless of the chosen functional, DFT tends to underestimate the band gap. Similarly, partially self-consistent GW_0 calculations generally yield smaller values. Our results align well with fully self-consistent GW calculations but tend to be slightly larger.

TABLE II. Comparison of band gap values (in eV) for three geometries of tPA, obtained using various methods. For DFT+TN, the results at range $R = 4$ are reported.

Method	tPA1	tPA2	tPA3
PBE	0.001	0.247	0.718
HSE06	0.231	0.602	1.242
B3LYP	0.531	0.914	1.572
GW_0	1.152	2.076	3.033
GW	1.711	2.838	4.012
EOM-CCSD [123]			4.941
DFT+TN	2.09	3.15	4.28

B. Polythiophene

1. Downfolding

PT, illustrated in Fig. 1b, has a more complex structure than tPA. Again, we start from a DFT calculation to obtain the Kohn-Sham eigenvalues. From the resulting band structure (see Fig. 5), a band gap of 1.1 eV is observed at the Γ -point. The π orbitals exhibit noticeable hybridization, leading to electron delocalization. To construct sufficiently localized Wannier functions, we focus on the target space spanned by the six p_z bands associated with two sulfur and four carbon atoms. As shown in Fig. 5, the Wannier-interpolated bands accurately reproduce the four highest valence bands and the two lowest conduction bands. The effective model consists of six bands, a relatively large number compared to typical tight-binding or low-energy models. This results in a filling of eight electrons distributed among six orbitals, highlighting the complexity of the system.

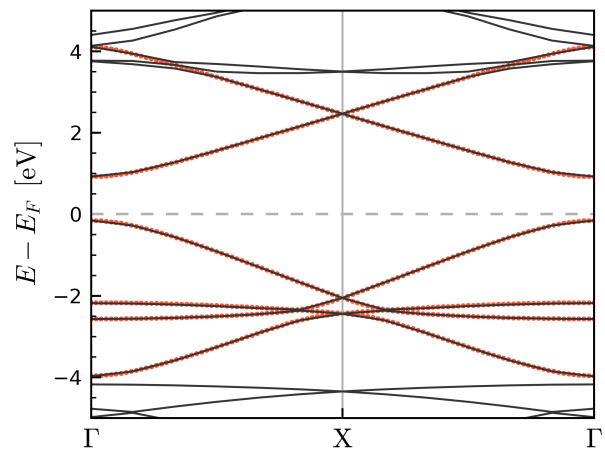


FIG. 5. The electronic band structure of polythiophene, with the Fermi energy E_F shifted to 0 eV. The dotted lines are the Wannier interpolated bands. The high-symmetry points of the Brillouin zone are labeled by $\Gamma = (0,0,0)$ and $X = (0.5,0,0)$.

In Table III, the parameters defining the Hubbard model are presented. We include all the on-site ($[0,0,0]$) and nearest-neighbor ($[1,0,0]$) hopping and direct interaction terms. Compared to tPA, inter-site interactions are neglected at shorter distances within the lattice, which is justified by the larger physical size of the PT unit cell. To reduce the computational cost, the remaining interactions, such as exchange terms, are also omitted.

2. Model solution

Experiments on bulk PT samples have reported a band gap of approximately 2.0 eV [85]. However, direct mea-

TABLE III. Hopping matrices $t_{ij}^{\alpha\beta}$ from tight-binding approximation with Hartree correction and direct Coulomb interaction $U_{ij}^{\alpha\beta}$ from cRPA for PT. The elements (in eV) correspond to the hopping/interaction parameter between band α on site $\mathbf{R}_i = [0, 0, 0]$ (rows) and band β on different sites $\mathbf{R}_j = [j, 0, 0]$ (columns).

t											
[0,0,0]						[1,0,0]					
0.957	1.919	-0.944	-0.976	-0.048	-0.033	0.015	0.098	-0.050	0.008	-0.038	-0.037
1.919	0.000	1.726	-1.969	-0.474	1.300	0.275	-0.126	0.192	-0.023	0.085	0.138
-0.944	1.726	1.741	0.665	-0.417	-0.654	-0.038	0.216	-0.117	0.000	-0.083	-0.081
-0.976	-1.969	0.665	1.386	1.099	1.011	0.244	-0.053	0.111	0.012	0.037	0.040
-0.048	-0.474	-0.417	1.099	2.595	-0.990	-2.099	0.211	-0.536	-0.052	-0.052	-0.183
-0.033	1.300	-0.654	1.011	-0.990	1.636	-1.003	0.587	-0.462	-0.113	-0.077	-0.133
U											
[0,0,0]						[1,0,0]					
5.642	4.055	4.630	3.323	2.344	2.122	1.590	1.121	1.148	0.872	0.670	0.630
4.055	5.857	4.814	4.540	3.435	3.156	2.454	1.676	1.708	1.300	0.989	0.925
4.630	4.813	6.051	4.713	3.292	2.911	2.135	1.458	1.501	1.143	0.876	0.822
3.323	4.540	4.713	6.147	5.019	4.310	2.998	1.946	2.038	1.527	1.158	1.077
2.344	3.436	3.293	5.020	6.064	5.299	4.273	2.751	2.889	2.132	1.579	1.453
2.122	3.156	2.911	4.311	5.299	6.044	4.650	2.836	3.024	2.222	1.630	1.504

measurements on true single chains are not available in the literature. Given the relatively weak electron correlation suggested by the delocalized nature of the π electrons, *GW* calculations may serve as a reliable benchmark for comparison.

From the six-band Hubbard model described above, a band gap of 2.94 eV is obtained at momentum $k = 0$, with convergence achieved at bond lengths above 300 (see Appendix D). This result shows good agreement with the single-shot G_0W_0 calculation (see Table IV), while fully self-consistent *GW* predicts a value 0.65 eV higher. Although the effective model neglects exchange and longer-range interactions, our methodology aligns more closely with *GW* calculations than hybrid DFT functionals such as HSE06 [125] and B3LYP. This suggests that even with its simplifications, the model captures essential electronic properties more effectively than commonly used exchange-correlation functionals. That said, the delocalized nature of the electrons and relatively weak electron correlation make this material less ideal for this approach, as strong localization effects typically enhance the accuracy of such models. Nonetheless, we demonstrate that it remains effective in describing the system's fundamental electronic features.

TABLE IV. Comparison of band gap values for a single chain of PT obtained using various methods.

Method	E_g [eV]	Reference
PBE	1.1	Current work
HSE06	2.0	[126]
B3LYP	2.08	[127]
G_0W_0	3.10	[128]
<i>GW</i>	3.59	[129]
DFT+TN	2.94	Current work

C. Sr_2CuO_3

1. Downfolding

The quasi-1D material Sr_2CuO_3 , shown in Fig. 1c, contains 1D CuO_3 chains. DFT calculations in VASP on a $7 \times 5 \times 9$ k -mesh produce the band structure given in Fig. 6. The bands crossing the Fermi energy originate from copper $d_{x^2-y^2}$ orbitals. A supercell containing four copper atoms was necessary to access nearest-neighbor interaction parameters in VASP, so that four such copper $d_{x^2-y^2}$ bands are present in the band structure. Single chains can then be considered as one-band Hubbard models at half-filling. The derived model parameters for Sr_2CuO_3 can be found in Table V and are all taken into account. The on-site hopping term is a constant chemical potential, which does not affect the physical properties since the number of electrons is fixed. Due to technical complications (see Section VB), the Hartree double-counting corrections (13) cannot be determined and are therefore omitted in this case. The direct interactions only contribute to a shift in the chemical potential, which is not physically relevant. Since both J_{01} and \tilde{U}_{01} are already small, the correction terms are expected to be negligible, justifying the approximation.

2. Model solution

In Fig. 7, the staggered magnetization, $m_s = \langle |n_\uparrow - n_\downarrow| \rangle$, of the ground state is plotted as a function of the bond dimension. At first glance, it appears to converge toward a small but nonzero value, suggesting the presence of antiferromagnetism within the chain. However, the existence of antiferromagnetic order in a

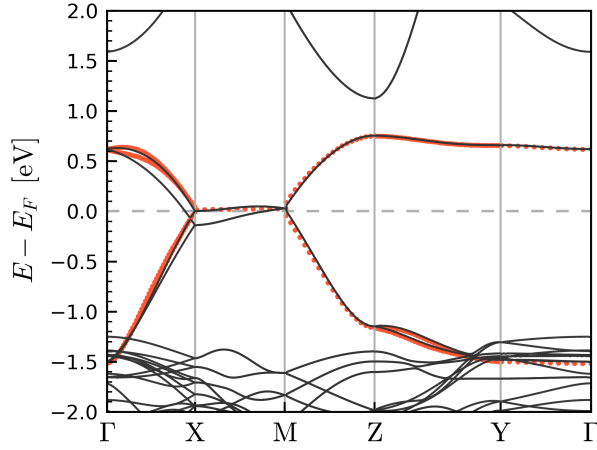


FIG. 6. The electronic band structure of Sr_2CuO_3 , with the Fermi energy E_F shifted to 0 eV. The dotted lines are the Wannier interpolated bands. An orthorhombic supercell containing four times the structure formula has been used. The high-symmetry points of the Brillouin zone are labeled by $\Gamma = (0, 0, 0)$, $X = (0.5, 0, 0)$, $M = (0.5, 0, 0.5)$, $Z = (0, 0, 0.5)$, and $Y = (0, 0.5, 0)$.

TABLE V. Hopping parameters t_{ij} from tight-binding approximation, direct Coulomb interaction U_{ij} , exchange J_{ij} , and $\tilde{U}_{ij} = U_{ijjj} = U_{jijj} = U_{jjji} = U_{jjji}$ from cRPA for Sr_2CuO_3 . The elements (in eV) correspond to the parameter between site $\mathbf{R}_i = [0, 0, 0]$ and sites $\mathbf{R}_j = [j, 0, 0]$ (columns).

t			
$[0, 0, 0]$	$[1, 0, 0]$	$[2, 0, 0]$	$[3, 0, 0]$
0.130	0.486	0.077	0.018
U		J	\tilde{U}
$[0, 0, 0]$	$[1, 0, 0]$	$[1, 0, 0]$	$[1, 0, 0]$
3.391	1.049	0.031	-0.033

purely 1D $SU(2)$ -invariant spin chain is ruled out by the Hohenberg-Mermin-Wagner theorem [130–132], or more precisely, by its zero-temperature extension [133]. It is well known, however, that MPS simulations tend to develop such order and break the symmetry as a means of reducing entanglement, though the symmetry should be restored in the limit of increasing bond dimension. The experimentally observed antiferromagnetism must therefore be a consequence of spin-orbit or interchain coupling, and the precise value of the order parameter cannot be predicted with the current approach.

A second property of interest is the band gap. Experimentally, band gaps of 1.5 eV [134] and 1.77 eV [135] have been reported. The band gap obtained from the one-band Hubbard model is located at momentum $k = \pi$. As the bond dimension increases, it converges to 1.57 eV, closely matching the experimental result reported by Maiti et al. [134].

Future work may incorporate oxygen p -bands into the effective model to explore the role of charge transfer

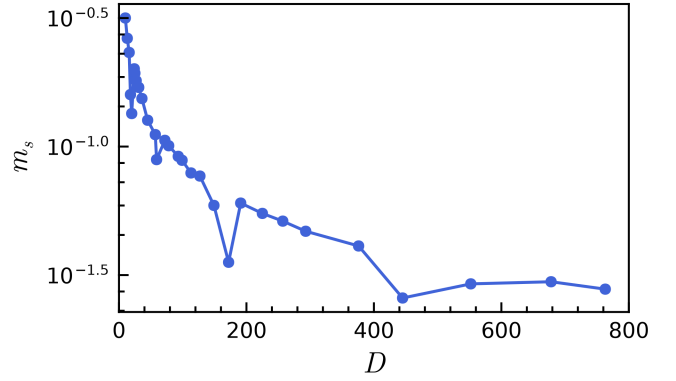


FIG. 7. The staggered magnetization as a function of the bond dimension for the effective Hubbard model of Sr_2CuO_3 .

between copper and oxygen orbitals. However, including oxygen p -orbitals in a multi-band model remains challenging due to their strong entanglement with high-energy states. In such cases, the static limit approximation becomes insufficient, necessitating an investigation of frequency renormalization corrections. These challenges will be addressed in future studies, along with cGW calculations to eliminate exchange-correlation double counting.

IV. CONCLUSION AND OUTLOOK

We have developed a novel approach for simulating strongly correlated materials and applied it to three distinct systems. The methodology begins with a cost-effective DFT calculation to determine the material's electronic band structure, followed by identifying an appropriate low-energy target space. After constructing the Wannier functions spanning this space, the Hubbard interaction parameters are extracted using cRPA. To correct for the double counting of interaction terms inherent in the DFT energy functional, an additional calculation is performed to adjust the hopping parameters. In this work, we corrected for the Hartree term, while ongoing research focuses on implementing cGW to eliminate double counting arising from the exchange-correlation functional. The resulting hopping and interaction parameters define an effective Hubbard model that captures the system's essential low-energy physics.

In the second stage, relevant observables are computed from the Hubbard model. Tensor networks have proven to be a suitable computational tool for this purpose, demonstrated by the application of MPS to one-dimensional and quasi-one-dimensional materials.

We studied several effective models of increasing complexity for three geometries of trans-polyacetylene. The flexibility of tensor networks allowed for the implementation of longer-range Hamiltonians, including interaction terms involving three ($U_{ijk}^{\alpha\beta\gamma\gamma}$) or four ($U_{ijkl}^{\alpha\beta\gamma\delta}$) orbitals,

while maintaining computational feasibility. The computed band gap lies between the results of state-of-the-art computational approaches, *GW* and EOM-CCSD, validating the method. The geometry without significant BLA led to the gap closest to the experimental value, suggesting that the alternation in experiments is rather small.

For polythiophene, the low-energy space was represented by a six-band Hubbard model with a filling of $8/6$. Despite its complexity, the model allowed for the inclusion of inter-site interactions, demonstrating the efficient scaling of our approach. The predicted band gap was consistent with *GW* calculations, outperforming popular hybrid DFT functionals.

Finally, we applied our method to a quasi-one-dimensional material, Sr_2CuO_3 , using a one-band Hubbard model. While this model cannot conclusively predict antiferromagnetism, the Hohenberg-Mermin-Wagner theorem and its extensions suggest that antiferromagnetic order emerges due to spin-orbit interactions or inter-chain coupling. On the other hand, the computed Mott gap closely matched experimental observations.

The combination of downfolding techniques and tensor network methods provides accurate predictions of material properties while maintaining computational efficiency. Additionally, this framework is highly adaptable, enabling the implementation of complex Hamiltonians. The one-dimensional examples presented here serve as a proof of concept, demonstrating the feasibility of extending the approach to higher dimensions using PEPS instead of MPS. Future work will explore the frequency dependence of the Hubbard parameters and investigate additional properties such as strong spin-orbit coupling.

V. COMPUTATIONAL DETAILS

The computational methods employed in this study are detailed below. All input files can be found in the GitHub repository [136] to ensure reproducibility.

A. Structure relaxation

Geometry relaxation is performed using VASP [137, 138] with the projector augmented-wave method [139]. For tPA1 and tPA2, the PBE [99] and B3LYP [21] functionals are used, respectively, with a 20 \AA vacuum layer to isolate the chains. A plane-wave energy cutoff of 600 eV is applied on a $15 \times 1 \times 1$ k -grid along the chain axis. Electronic minimization proceeds until the energy difference falls below 10^{-8} eV , while structural relaxation continues until forces converge to 10^{-6} eV . See Appendix A for the resulting energy surface.

The geometry of PT is optimized following a similar approach to tPA1, with relaxation considered complete when atomic forces are reduced below 0.01 eV/\AA .

For Sr_2CuO_3 , structural optimization is carried out using the PBE functional on a $7 \times 5 \times 9$ k -mesh. Convergence criteria include an electronic energy tolerance of 10^{-9} eV and an energy threshold of 10^{-8} eV . A plane-wave cutoff of 600 eV is applied, along with Gaussian smearing for electronic occupation.

B. Downfolding

Downfolding for tPA and PT is performed via 1D DFT calculations in PySCF [140], employing the PBE functional. For tPA, the all-electron correlation-consistent polarized valence triple-zeta (cc-pVTZ) basis set [141] is used, while for PT, the pseudopotential GTH-DZVP basis from the CP2K software package [142] is applied. MLWFs are constructed using Wannier90 [143], and interaction and hopping parameters are extracted via an in-house cRPA implementation [136].

For tPA, the initial DFT calculation is performed with 28 k -points along the chain to ensure parameter convergence, while for PT, 12 k -points are used. The direct interactions exhibit a slow convergence with respect to the number of k -points, following a $1/N_k$ dependence (see Appendix B). This behavior arises from the Coulomb divergence in the Gaussian density fitting scheme implemented in PySCF [144, 145]. As proposed by Berkelbach and coworkers [145], we extrapolated these parameters based on a reliable fit. The hopping and other interaction parameters do not suffer from this issue.

Since Sr_2CuO_3 is significantly more complex than the other two cases, performing a self-consistent field computation on a sufficiently dense k -grid is not yet feasible in PySCF. To address this limitation, we prioritize computational efficiency over some of PySCF's flexible features by using VASP instead. Downfolding for Sr_2CuO_3 is carried out in VASP using the PBE functional on a $7 \times 5 \times 9$ k -mesh, with a plane-wave cutoff of 600 eV . The cRPA algorithm implemented in VASP is employed, but double-counting corrections are not applied because Coulomb interactions can only be computed among maximally localized Wannier functions (MLWFs) within the chosen unit cell. To properly capture nearest-neighbor interactions, an orthorhombic supercell is used.

C. Tensor network calculations

For the calculation of the Hubbard model, we utilized the open-source packages TensorKit.jl [146], MPSKit.jl [147], and MPSKitModels.jl, all developed in the Julia programming language. These packages offer efficient implementations of various tensor network algorithms, including support for symmetries and fermionic features.

The lattice of the model is represented as an infinite chain of matrix product states, arranged in a zigzag pattern to form an infinite strip of a specific width. For a Hubbard model with B bands, this strip has a width of

B sites, meaning that the different orbitals are modeled as separate sites within the unit cell. Additionally, several symmetries are imposed on the states to restrict the degrees of freedom and reduce computational cost. We utilize the \mathbb{Z}_2 symmetry, derived from the fermionic nature of electrons, an $SU(2)$ spin symmetry, and a $U(1)$ symmetry to conserve the total number of electrons. If we are interested in the spin configuration and an explicit distinction between spin up and spin down has to be made, as is the case for the study of antiferromagnetism in Sr_2CuO_3 , the $SU(2)$ symmetry is replaced with another $U(1)$ symmetry to separately conserve the number of spin-up and spin-down electrons.

For a system with filling $f = P/Q$, i.e. P electrons per Q orbitals, the quantum numbers of the particle-conserving $U(1)$ symmetry are shifted and rescaled from 0,1,2 for an unoccupied, singly occupied, and doubly occupied orbital to $-P$, $Q - P$, and $2Q - P$, respectively. To ensure the injectivity of the MPS, the unit cell must be extended to Q sites if P is even and $2Q$ sites if P is odd [117]. Consequently, a B -band model with filling P/Q requires a unit cell of size BQ or $2BQ$.

Once the Hamiltonian is constructed, infinite two-site DMRG is performed to compute the ground state of the system while dynamically determining the bond dimen-

sion, followed by several VUMPS iterations to guarantee convergence. The relative tolerance is set to 10^{-6} . Excitations on top of the ground state are determined using the quasiparticle algorithm, as introduced by Haegeman et al. [115]. We look for the first particle and hole excitation as a function of the momentum and identify their sum as the required energy to create a free electron-hole pair. The band gap of the model is then extracted as the minimum. Excitons, on the other hand, correspond to excitations in the trivial sector.

ACKNOWLEDGMENTS

This work is supported by the Research Board of Ghent University (BOF) through a Concerted Research Action (BOF23/GOA/021). V. V. S. acknowledges the Research Board of Ghent University (BOF). J. H. and L. D. acknowledge the Fund for Scientific Research-Flanders (FWO) via grant no. 3G011920 and no. 3G0E1820, respectively. The computational resources (Stevin Supercomputer Infrastructure) and services used in this work were provided by VSC (Flemish Supercomputer Center), funded by Ghent University, FWO, and the Flemish Government—department EWI.

-
- [1] P. Hohenberg and W. Kohn, Inhomogeneous electron gas, *Phys. Rev.* **136**, B864 (1964).
 - [2] W. Kohn and L. J. Sham, Self-consistent equations including exchange and correlation effects, *Phys. Rev.* **140**, A1133 (1965).
 - [3] J. Hafner, C. M. Wolverton, and G. Ceder, Toward computational materials design: The impact of density functional theory on materials research, *MRS Bulletin* **31**, 659 (2006).
 - [4] J. Neugebauer and T. Hickel, Density functional theory in materials science, *WIREs Computational Molecular Science* **3**, 438 (2013).
 - [5] E. Morosan, D. Natelson, A. H. Nevidomskyy, and Q. Si, Strongly correlated materials, *Advanced Materials* **24**, 4896 (2012).
 - [6] P. R. C. Kent and G. Kotliar, Toward a predictive theory of correlated materials, *Science* **361**, 348 (2018).
 - [7] J. G. Bednorz and K. A. Müller, Possible high- T_c superconductivity in the Ba-La-Cu-O system, *Zeitschrift für Physik B Condensed Matter* **64**, 189 (1986).
 - [8] L. F. Mattheiss, Electronic band properties and superconductivity in $\text{La}_{2-y}\text{X}_y\text{CuO}_4$, *Phys. Rev. Lett.* **58**, 1028 (1987).
 - [9] M. S. Hybertsen, M. Schlüter, and N. E. Christensen, Calculation of coulomb-interaction parameters for La_2CuO_4 using a constrained-density-functional approach, *Phys. Rev. B* **39**, 9028 (1989).
 - [10] D. Li, K. Lee, B. Y. Wang, M. Osada, S. Crossley, H. R. Lee, Y. Cui, Y. Hikita, and H. Y. Hwang, Superconductivity in an infinite-layer nickelate, *Nature* **572**, 624 (2019).
 - [11] D. Li, B. Y. Wang, K. Lee, S. P. Harvey, M. Osada, B. H. Goodge, L. F. Kourkoutis, and H. Y. Hwang, Superconducting dome in $\text{Nd}_{1-x}\text{Sr}_x\text{NiO}_2$ infinite layer films, *Phys. Rev. Lett.* **125**, 027001 (2020).
 - [12] S. Zeng, C. Li, L. E. Chow, Y. Cao, Z. Zhang, C. S. Tang, X. Yin, Z. S. Lim, J. Hu, P. Yang, *et al.*, Superconductivity in infinite-layer nickelate $\text{La}_{1-x}\text{Ca}_x\text{NiO}_2$ thin films, *Science Advances* **8**, eabl9927 (2022).
 - [13] S. Jin, T. H. Tiesel, M. McCormack, R. A. Fastnacht, R. Ramesh, and L. H. Chen, Thousandfold change in resistivity in magnetoresistive La-Ca-Mn-O films, *Science* **264**, 413 (1994).
 - [14] E. Dagotto, T. Hotta, and A. Moreo, Colossal magnetoresistant materials: the key role of phase separation, *Physics Reports* **344**, 1 (2001).
 - [15] E. Dagotto, Complexity in strongly correlated electronic systems, *Science* **309**, 257 (2005).
 - [16] E. J. W. Verwey, Electronic conduction of magnetite (Fe_3O_4) and its transition point at low temperatures, *Nature* **144**, 327 (1939).
 - [17] M. Imada, A. Fujimori, and Y. Tokura, Metal-insulator transitions, *Rev. Mod. Phys.* **70**, 1039 (1998).
 - [18] H. Jiang, First-principles approaches for strongly correlated materials: A theoretical chemistry perspective, *International Journal of Quantum Chemistry* **115**, 722 (2015).
 - [19] V. I. Anisimov, J. Zaanen, and O. K. Andersen, Band theory and Mott insulators: Hubbard U instead of Stoner I , *Phys. Rev. B* **44**, 943 (1991).
 - [20] V. I. Anisimov, F. tianwan, and A. I. Lichtenstein, First-principles calculations of the electronic structure and spectra of strongly correlated systems: the LDA+ U method, *Journal of Physics: Condensed Matter* **9**, 767

- (1997).
- [21] A. D. Becke, A new mixing of Hartree–Fock and local density-functional theories, *The Journal of Chemical Physics* **98**, 1372 (1993).
 - [22] J. P. Perdew, M. Ernzerhof, and K. Burke, Rationale for mixing exact exchange with density functional approximations, *The Journal of Chemical Physics* **105**, 9982 (1996).
 - [23] L. Hedin, New method for calculating the one-particle Green’s function with application to the electron-gas problem, *Phys. Rev.* **139**, A796 (1965).
 - [24] L. Hedin and S. Lundqvist, Effects of electron-electron and electron-phonon interactions on the one-electron states of solids (Academic Press, 1970) pp. 1–181.
 - [25] F. Aryasetiawan and F. Nilsson, Downfolding methods in many-electron theory.
 - [26] H. Jiang, R. I. Gomez-Abal, P. Rinke, and M. Scheffler, First-principles modeling of localized d states with the $GW@LDA+U$ approach, *Phys. Rev. B* **82**, 045108 (2010).
 - [27] F. Aryasetiawan and O. Gunnarsson, Electronic structure of NiO in the GW approximation, *Phys. Rev. Lett.* **74**, 3221 (1995).
 - [28] H. Jiang, P. Rinke, and M. Scheffler, Electronic properties of lanthanide oxides from the GW perspective, *Phys. Rev. B* **86**, 125115 (2012).
 - [29] I. Shavitt and R. J. Bartlett, *Many-Body Methods in Chemistry and Physics: MBPT and Coupled-Cluster Theory*, Cambridge Molecular Science (Cambridge University Press, 2009).
 - [30] R. J. Bartlett and M. Musial, Coupled-cluster theory in quantum chemistry, *Rev. Mod. Phys.* **79**, 291 (2007).
 - [31] P. Knowles and N. Handy, A new determinant-based full configuration interaction method, *Chemical Physics Letters* **111**, 315 (1984).
 - [32] J. Hubbard and B. H. Flowers, Electron correlations in narrow energy bands, *Proceedings of the Royal Society of London. Series A. Mathematical and Physical Sciences* **276**, 238 (1963).
 - [33] O. Kristanovski, A. B. Shick, F. Lechermann, and A. I. Lichtenstein, Role of nonspherical double counting in DFT+DMFT: Total energy and structural optimization of pnictide superconductors, *Phys. Rev. B* **97**, 201116 (2018).
 - [34] C. Falter and M. Selmke, Renormalization of the dielectric response with applications to effective ion interactions and phonons, *Phys. Rev. B* **24**, 586 (1981).
 - [35] P. H. Dederichs, S. Blügel, R. Zeller, and H. Akai, Ground states of constrained systems: Application to cerium impurities, *Phys. Rev. Lett.* **53**, 2512 (1984).
 - [36] A. K. McMahan, R. M. Martin, and S. Satpathy, Calculated effective hamiltonian for La_2CuO_4 and solution in the impurity anderson approximation, *Phys. Rev. B* **38**, 6650 (1988).
 - [37] C. Falter, A unifying approach to lattice dynamical and electronic properties of solids, *Physics Reports* **164**, 1 (1988).
 - [38] Z. Zhang and S. Satpathy, Electron states, magnetism, and the verwey transition in magnetite, *Phys. Rev. B* **44**, 13319 (1991).
 - [39] M. Hirayama, T. Miyake, and M. Imada, Derivation of static low-energy effective models by an ab initio downfolding method without double counting of coulomb correlations: Application to SrVO_3 , fese, and fete, *Phys. Rev. B* **87**, 195144 (2013).
 - [40] Y. Nomura and R. Arita, Ab initio downfolding for electron-phonon-coupled systems: Constrained density-functional perturbation theory, *Phys. Rev. B* **92**, 245108 (2015).
 - [41] F. Aryasetiawan, M. Imada, A. Georges, G. Kotliar, S. Biermann, and A. I. Lichtenstein, Frequency-dependent local interactions and low-energy effective models from electronic structure calculations, *Phys. Rev. B* **70**, 195104 (2004).
 - [42] F. Aryasetiawan, K. Karlsson, O. Jepsen, and U. Schönberger, Calculations of Hubbard U from first-principles, *Phys. Rev. B* **74**, 125106 (2006).
 - [43] S. Biermann, Dynamical screening effects in correlated electron materials—a progress report on combined many-body perturbation and dynamical mean field theory: ‘GW + DMFT’, *Journal of Physics: Condensed Matter* **26**, 173202 (2014).
 - [44] N. Sheng, C. Vorwerk, M. Govoni, and G. Galli, Green’s function formulation of quantum defect embedding theory, *Journal of Chemical Theory and Computation* **18**, 3512 (2022).
 - [45] L. Muechler, D. I. Badrtdinov, A. Hampel, J. Cano, M. Rösner, and C. E. Dreyer, Quantum embedding methods for correlated excited states of point defects: Case studies and challenges, *Phys. Rev. B* **105**, 235104 (2022).
 - [46] K. Haule, Exact double counting in combining the dynamical mean field theory and the density functional theory, *Phys. Rev. Lett.* **115**, 196403 (2015).
 - [47] G. Kotliar, S. Y. Savrasov, K. Haule, V. S. Oudovenko, O. Parcollet, and C. A. Marianetti, Electronic structure calculations with dynamical mean-field theory, *Rev. Mod. Phys.* **78**, 865 (2006).
 - [48] Y. Chang, E. G. C. P. van Loon, B. Eskridge, B. Busemeyer, M. A. Morales, C. E. Dreyer, A. J. Millis, S. Zhang, T. O. Wehling, L. K. Wagner, *et al.*, Downfolding from ab initio to interacting model hamiltonians: comprehensive analysis and benchmarking of the DFT+cRPA approach, *npj Computational Materials* **10**, 129 (2024).
 - [49] W. Metzner and D. Vollhardt, Correlated lattice fermions in $d = \infty$ dimensions, *Phys. Rev. Lett.* **62**, 324 (1989).
 - [50] A. Georges, G. Kotliar, W. Krauth, and M. J. Rozenberg, Dynamical mean-field theory of strongly correlated fermion systems and the limit of infinite dimensions, *Rev. Mod. Phys.* **68**, 13 (1996).
 - [51] P. W. Anderson, Localized magnetic states in metals, *Phys. Rev.* **124**, 41 (1961).
 - [52] S. Zhang and H. Krakauer, Quantum monte carlo method using phase-free random walks with slater determinants, *Phys. Rev. Lett.* **90**, 136401 (2003).
 - [53] J. Gubernatis, N. Kawashima, and P. Werner, *Quantum Monte Carlo Methods: Algorithms for Lattice Models* (Cambridge University Press, 2016).
 - [54] K. Held, Electronic structure calculations using dynamical mean field theory, *Advances in Physics* **56**, 829 (2007).
 - [55] A. I. Lichtenstein and M. I. Katsnelson, Ab initio calculations of quasiparticle band structure in correlated systems: LDA++ approach, *Phys. Rev. B* **57**, 6884 (1998).
 - [56] P. Sun and G. Kotliar, Extended dynamical mean-field theory and GW method, *Phys. Rev. B* **66**, 085120

- (2002).
- [57] S. Biermann, F. Aryasetiawan, and A. Georges, First-principles approach to the electronic structure of strongly correlated systems: Combining the *GW* approximation and dynamical mean-field theory, *Phys. Rev. Lett.* **90**, 086402 (2003).
 - [58] L. Boehnke, F. Nilsson, F. Aryasetiawan, and P. Werner, When strong correlations become weak: Consistent merging of *GW* and DMFT, *Phys. Rev. B* **94**, 201106 (2016).
 - [59] F. Nilsson, L. Boehnke, P. Werner, and F. Aryasetiawan, Multitier self-consistent *GW* + EDMFT, *Phys. Rev. Mater.* **1**, 043803 (2017).
 - [60] M. H. Hettler, A. N. Tahvildar-Zadeh, M. Jarrell, T. Pruschke, and H. R. Krishnamurthy, Nonlocal dynamical correlations of strongly interacting electron systems, *Phys. Rev. B* **58**, R7475 (1998).
 - [61] A. I. Lichtenstein and M. I. Katsnelson, Antiferromagnetism and d-wave superconductivity in cuprates: A cluster dynamical mean-field theory, *Phys. Rev. B* **62**, R9283 (2000).
 - [62] G. Kotliar, S. Y. Savrasov, G. Pálsson, and G. Biroli, Cellular dynamical mean field approach to strongly correlated systems, *Phys. Rev. Lett.* **87**, 186401 (2001).
 - [63] A. Galler, P. Thunström, J. Kaufmann, M. Pickem, J. M. Tomczak, and K. Held, The abinitioDFA project v1.0: Non-local correlations beyond and susceptibilities within dynamical mean-field theory, *Computer Physics Communications* **245**, 106847 (2019).
 - [64] A. N. Rubtsov, M. I. Katsnelson, and A. I. Lichtenstein, Dual fermion approach to nonlocal correlations in the Hubbard model, *Phys. Rev. B* **77**, 033101 (2008).
 - [65] A. Rubtsov, M. Katsnelson, and A. Lichtenstein, Dual boson approach to collective excitations in correlated fermionic systems, *Annals of Physics* **327**, 1320 (2012).
 - [66] G. Rohringer, A. Toschi, H. Hafermann, K. Held, V. I. Anisimov, and A. A. Katanin, One-particle irreducible functional approach: A route to diagrammatic extensions of the dynamical mean-field theory, *Phys. Rev. B* **88**, 115112 (2013).
 - [67] C. Taranto, S. Andergassen, J. Bauer, K. Held, A. Katanin, W. Metzner, G. Rohringer, and A. Toschi, From infinite to two dimensions through the functional renormalization group, *Phys. Rev. Lett.* **112**, 196402 (2014).
 - [68] T. Ayral and O. Parcollet, Mott physics and spin fluctuations: A unified framework, *Phys. Rev. B* **92**, 115109 (2015).
 - [69] G. Li, Hidden physics in the dual-fermion approach: A special case of a nonlocal expansion scheme, *Phys. Rev. B* **91**, 165134 (2015).
 - [70] G. Rohringer, H. Hafermann, A. Toschi, A. A. Katanin, A. E. Antipov, M. I. Katsnelson, A. I. Lichtenstein, A. N. Rubtsov, and K. Held, Diagrammatic routes to nonlocal correlations beyond dynamical mean field theory, *Rev. Mod. Phys.* **90**, 025003 (2018).
 - [71] G. Knizia and G. K.-L. Chan, Density matrix embedding: A simple alternative to dynamical mean-field theory, *Phys. Rev. Lett.* **109**, 186404 (2012).
 - [72] D. Zgid and E. Gull, Finite temperature quantum embedding theories for correlated systems, *New Journal of Physics* **19**, 023047 (2017).
 - [73] C.-N. Yeh, S. Isakov, D. Zgid, and E. Gull, Electron correlations in the cubic paramagnetic perovskite $\text{Sr}(\text{V}, \text{Mn})\text{O}_3$: Results from fully self-consistent self-energy embedding calculations, *Phys. Rev. B* **103**, 195149 (2021).
 - [74] E. Y. Loh, J. E. Gubernatis, R. T. Scalettar, S. R. White, D. J. Scalapino, and R. L. Sugar, Sign problem in the numerical simulation of many-electron systems, *Phys. Rev. B* **41**, 9301 (1990).
 - [75] J. I. Cirac, D. Pérez-García, N. Schuch, and F. Verstraete, Matrix product states and projected entangled pair states: Concepts, symmetries, theorems, *Rev. Mod. Phys.* **93**, 045003 (2021).
 - [76] F. Verstraete and J. I. Cirac, Renormalization algorithms for quantum-many body systems in two and higher dimensions (2004), arXiv:cond-mat/0407066 [cond-mat.str-el].
 - [77] S. R. White, Density matrix formulation for quantum renormalization groups, *Phys. Rev. Lett.* **69**, 2863 (1992).
 - [78] U. Schollwöck, The density-matrix renormalization group in the age of matrix product states, *Annals of Physics* **326**, 96 (2011), january 2011 Special Issue.
 - [79] M. Fannes, B. Nachtergaele, and R. F. Werner, Finitely correlated states on quantum spin chains, *Communications in Mathematical Physics* **144**, 443 (1992).
 - [80] A. Klumper, A. Schadschneider, and J. Zittartz, Equivalence and solution of anisotropic spin-1 models and generalized t-J fermion models in one dimension, *Journal of Physics A: Mathematical and General* **24**, L955 (1991).
 - [81] A. Klumper, A. Schadschneider, and J. Zittartz, Matrix product ground states for one-dimensional spin-1 quantum antiferromagnets, *Europhysics Letters* **24**, 293 (1993).
 - [82] F. Verstraete and J. I. Cirac, Valence-bond states for quantum computation, *Phys. Rev. A* **70**, 060302 (2004).
 - [83] K. Müllen and U. Scherf, Conjugated polymers: Where we come from, where we stand, and where we might go, *Macromolecular Chemistry and Physics* **224**, 2200337 (2023).
 - [84] T. Tani, P. Grant, W. Gill, G. Street, and T. Clarke, Phototransport effects in polyacetylene, $(\text{CH})_x$, *Solid State Communications* **33**, 499 (1980).
 - [85] M. Kobayashi, J. Chen, T.-C. Chung, F. Moraes, A. Heeger, and F. Wudl, Synthesis and properties of chemically coupled poly(thiophene), *Synthetic Metals* **9**, 77 (1984).
 - [86] A. J. Heeger, S. Kivelson, J. R. Schrieffer, and W. P. Su, Solitons in conducting polymers, *Rev. Mod. Phys.* **60**, 781 (1988).
 - [87] G. Zotti, S. Martina, G. Wegner, and A.-D. Schlüter, Well-defined pyrrole oligomers: Electrochemical and UV/vis studies, *Advanced Materials* **4**, 798 (1992).
 - [88] S. Glenis, M. Benz, E. LeGoff, J. L. Schindler, C. R. Kannewurf, and M. G. Kanatzidis, Polyfuran: a new synthetic approach and electronic properties, *Journal of the American Chemical Society* **115**, 12519 (1993).
 - [89] U. Salzner, J. Lagowski, P. Pickup, and R. Poirier, Comparison of geometries and electronic structures of polyacetylene, polyborole, polycyclopentadiene, polypyrrole, polyfuran, polysilole, polyphosphole, polythiophene, polyselenophene and polytellurophene, *Synthetic Metals* **96**, 177 (1998).
 - [90] A. H. Malik, F. Habib, M. J. Qazi, M. A. Ganayee, Z. Ahmad, and M. A. Yattoo, A short review article on conjugated polymers, *Journal of Polymer Research* **30**,

- 115 (2023).
- [91] S. Wang, Q. Sun, O. Gröning, R. Widmer, C. A. Pignedoli, L. Cai, X. Yu, B. Yuan, C. Li, H. Ju, *et al.*, On-surface synthesis and characterization of individual polyacetylene chains, *Nature Chemistry* **11**, 924 (2019).
 - [92] C. L. Teske and H. Müller-Buschbaum, Über erdalkalimetall—oxocuprate. ii. zur kenntnis von Sr_2CuO_3 , *Zeitschrift für anorganische und allgemeine Chemie* **371**, 325 (1969).
 - [93] Z. Hiroi, M. Takano, M. Azuma, and Y. Takeda, A new family of copper oxide superconductors $\text{Sr}_{n+1}\text{Cu}_n\text{O}_{2n+1+\delta}$ stabilized at high pressure, *Nature* **364**, 315 (1993).
 - [94] E. H. Lieb and F. Y. Wu, Absence of Mott transition in an exact solution of the short-range, one-band model in one dimension, *Phys. Rev. Lett.* **20**, 1445 (1968).
 - [95] B. J. Kim, H. Koh, E. Rotenberg, S.-J. Oh, H. Eisaki, N. Motoyama, S. Uchida, T. Tohyama, S. Maekawa, Z.-X. Shen, *et al.*, Distinct spinon and holon dispersions in photoemission spectral functions from one-dimensional SrCuO_2 , *Nature Physics* **2**, 397 (2006).
 - [96] H. Fujisawa, T. Yokoya, T. Takahashi, S. Miyasaka, M. Kibune, and H. Takagi, Angle-resolved photoemission study of Sr_2CuO_3 , *Phys. Rev. B* **59**, 7358 (1999).
 - [97] Z. Chen, Y. Wang, S. N. Rebec, T. Jia, M. Hashimoto, D. Lu, B. Moritz, R. G. Moore, T. P. Devereaux, and Z.-X. Shen, Anomalous strong near-neighbor attraction in doped 1d cuprate chains, *Science* **373**, 1235 (2021).
 - [98] N. Marzari and D. Vanderbilt, Maximally localized generalized wannier functions for composite energy bands, *Phys. Rev. B* **56**, 12847 (1997).
 - [99] J. P. Perdew, K. Burke, and M. Ernzerhof, Generalized gradient approximation made simple, *Phys. Rev. Lett.* **77**, 3865 (1996).
 - [100] N. Marzari, A. A. Mostofi, J. R. Yates, I. Souza, and D. Vanderbilt, Maximally localized wannier functions: Theory and applications, *Rev. Mod. Phys.* **84**, 1419 (2012).
 - [101] F. Nilsson, R. Sakuma, and F. Aryasetiawan, Ab initio calculations of the Hubbard U for the early lanthanides using the constrained random-phase approximation, *Phys. Rev. B* **88**, 125123 (2013).
 - [102] T. Miyake, F. Aryasetiawan, and M. Imada, Ab initio procedure for constructing effective models of correlated materials with entangled band structure, *Phys. Rev. B* **80**, 155134 (2009).
 - [103] E. Şaşıoğlu, C. Friedrich, and S. Blügel, Effective coulomb interaction in transition metals from constrained random-phase approximation, *Phys. Rev. B* **83**, 121101 (2011).
 - [104] M. Kaltak, *Merging GW with DMFT*, Ph.D. thesis, Vienna (2015).
 - [105] M. Romanova, G. Weng, A. Apelian, and V. Vlček, Dynamical downfolding for localized quantum states, *npj Computational Materials* **9**, 126 (2023).
 - [106] C. J. C. Scott and G. H. Booth, Rigorous screened interactions for realistic correlated electron systems, *Phys. Rev. Lett.* **132**, 076401 (2024).
 - [107] M. Bockstedte, F. Schütz, T. Garratt, V. Ivády, and A. Gali, Ab initio description of highly correlated states in defects for realizing quantum bits, *npj Quantum Materials* **3**, 31 (2018).
 - [108] H. Ma, M. Govoni, and G. Galli, Quantum simulations of materials on near-term quantum computers, *npj Computational Materials* **6**, 85 (2020).
 - [109] D. Perez-Garcia, F. Verstraete, M. M. Wolf, and J. I. Cirac, Matrix product state representations (2007), arXiv:quant-ph/0608197 [quant-ph].
 - [110] G. Vidal, Efficient classical simulation of slightly entangled quantum computations, *Phys. Rev. Lett.* **91**, 147902 (2003).
 - [111] L. Vanderstraeten, J. Haegeman, and F. Verstraete, Tangent-space methods for uniform matrix product states, *SciPost Physics Lecture Notes* 10.21468/scipostphyslectnotes.7 (2019).
 - [112] U. Schollwöck, The density-matrix renormalization group, *Reviews of Modern Physics* **77**, 259–315 (2005).
 - [113] S. Wouters and D. Van Neck, The density matrix renormalization group for ab initio quantum chemistry, *The European Physical Journal D* **68**, 10.1140/epjd/e2014-50500-1 (2014).
 - [114] V. Zauner-Stauber, L. Vanderstraeten, M. T. Fishman, F. Verstraete, and J. Haegeman, Variational optimization algorithms for uniform matrix product states, *Phys. Rev. B* **97**, 045145 (2018).
 - [115] J. Haegeman, S. Michalakakis, B. Nachtergaele, T. J. Osborne, N. Schuch, and F. Verstraete, Elementary excitations in gapped quantum spin systems, *Phys. Rev. Lett.* **111**, 080401 (2013).
 - [116] J. Haegeman, T. J. Osborne, and F. Verstraete, Post-matrix product state methods: To tangent space and beyond, *Phys. Rev. B* **88**, 075133 (2013).
 - [117] V. Zauner-Stauber, L. Vanderstraeten, J. Haegeman, I. P. McCulloch, and F. Verstraete, Topological nature of spinons and holons: Elementary excitations from matrix product states with conserved symmetries, *Phys. Rev. B* **97**, 235155 (2018).
 - [118] T. Ito, H. Shirakawa, and S. Ikeda, Thermal cis–trans isomerization and decomposition of polyacetylene, *Journal of Polymer Science: Polymer Chemistry Edition* **13**, 1943 (1975).
 - [119] A. J. Heeger, Semiconducting and metallic polymers: the fourth generation of polymeric materials, *Current Applied Physics* **1**, 247 (2001).
 - [120] B. S. Hudson, Polyacetylene: Myth and reality, *Materials* **11**, 10.3390/ma11020242 (2018).
 - [121] Z. W. Windom, A. Perera, and R. J. Bartlett, Examining fundamental and excitation gaps at the thermodynamic limit: A combined (QTP) DFT and coupled cluster study on trans-polyacetylene and polyacene, *The Journal of Chemical Physics* **156**, 204308 (2022).
 - [122] Z. W. Windom, A. Lam, A. Perera, and R. J. Bartlett, An assessment of frozen natural orbitals and band gaps using equation of motion coupled cluster theory: a case study on polyacene and trans-polyacetylene (2024), arXiv:2402.08776 [physics.chem-ph].
 - [123] E. Moerman, A. Gallo, A. Irmeler, T. Schäfer, F. Hummel, A. Grüneis, and M. Scheffler, Finite-size effects in periodic EOM-CCSD for ionization energies and electron affinities: Convergence rate and extrapolation to the thermodynamic limit, *Journal of Chemical Theory and Computation* 10.1021/acs.jctc.4c01451 (2025).
 - [124] W. P. Su, J. R. Schrieffer, and A. J. Heeger, Solitons in polyacetylene, *Phys. Rev. Lett.* **42**, 1698 (1979).
 - [125] A. V. Krukau, O. A. Vydrov, A. F. Izmaylov, and G. E. Scuseria, Influence of the exchange screening parameter on the performance of screened hybrid functionals, *The*

- Journal of Chemical Physics **125**, 224106 (2006).
- [126] K. Sohlberg and M. E. Foster, What's the gap? a possible strategy for advancing theory, and an appeal for experimental structure data to drive that advance, *RSC Adv.* **10**, 36887 (2020).
 - [127] T. P. Kaloni, G. Schreckenbach, and M. S. Freund, Band gap modulation in polythiophene and polypyrrole-based systems, *Scientific Reports* **6**, 36554 (2016).
 - [128] G. Samsonidze, F. J. Ribeiro, M. L. Cohen, and S. G. Louie, Quasiparticle and optical properties of polythiophene-derived polymers, *Phys. Rev. B* **90**, 035123 (2014).
 - [129] J.-W. van der Horst, P. A. Bobbert, P. H. L. de Jong, M. A. J. Michels, G. Brocks, and P. J. Kelly, Ab initio prediction of the electronic and optical excitations in polythiophene: Isolated chains versus bulk polymer, *Phys. Rev. B* **61**, 15817 (2000).
 - [130] P. C. Hohenberg, Existence of long-range order in one and two dimensions, *Phys. Rev.* **158**, 383 (1967).
 - [131] N. D. Mermin and H. Wagner, Absence of ferromagnetism or antiferromagnetism in one- or two-dimensional isotropic heisenberg models, *Phys. Rev. Lett.* **17**, 1133 (1966).
 - [132] M. B. Walker and T. W. Ruijgrok, Absence of magnetic ordering in one and two dimensions in a many-band model for interacting electrons in a metal, *Phys. Rev.* **171**, 513 (1968).
 - [133] K. Tanaka, K. Takeda, and T. Idogaki, Absence of spontaneous symmetry breaking in the ground state of one-dimensional spin-orbital model, *Journal of Magnetism and Magnetic Materials* **272-276**, 908 (2004), proceedings of the International Conference on Magnetism (ICM 2003).
 - [134] K. Maiti, D. D. Sarma, T. Mizokawa, and A. Fujimori, Electronic structure of one-dimensional cuprates, *Phys. Rev. B* **57**, 1572 (1998).
 - [135] M. Ono, K. Miura, A. Maeda, H. Matsuzaki, H. Kishida, Y. Taguchi, Y. Tokura, M. Yamashita, and H. Okamoto, Linear and nonlinear optical properties of one-dimensional Mott insulators consisting of Nihalogen chain and CuO-chain compounds, *Phys. Rev. B* **70**, 085101 (2004).
 - [136] See repository at <https://github.com/DaanVrancken/Supporting-Info> for input files of calculations.
 - [137] G. Kresse and J. Hafner, Ab initio molecular dynamics for liquid metals, *Phys. Rev. B* **47**, 558 (1993).
 - [138] G. Kresse and J. Furthmüller, Efficient iterative schemes for ab initio total-energy calculations using a plane-wave basis set, *Phys. Rev. B* **54**, 11169 (1996).
 - [139] P. E. Blöchl, Projector augmented-wave method, *Phys. Rev. B* **50**, 17953 (1994).
 - [140] Q. Sun, X. Zhang, S. Banerjee, P. Bao, M. Barbry, N. S. Blunt, N. A. Bogdanov, G. H. Booth, J. Chen, Z.-H. Cui, *et al.*, Recent developments in the PySCF program package, *The Journal of Chemical Physics* **153**, 024109 (2020).
 - [141] T. H. Dunning Jr., Gaussian basis sets for use in correlated molecular calculations. I. the atoms boron through neon and hydrogen, *The Journal of Chemical Physics* **90**, 1007 (1989).
 - [142] T. D. Kühne, M. Iannuzzi, M. Del Ben, V. V. Rybkin, P. Seewald, F. Stein, T. Laino, R. Z. Khaliullin, O. Schütt, F. Schiffmann, *et al.*, CP2K: An electronic structure and molecular dynamics software package - quickstep: Efficient and accurate electronic structure calculations, *The Journal of Chemical Physics* **152**, 194103 (2020).
 - [143] G. Pizzi, V. Vitale, R. Arita, S. Blügel, F. Freimuth, G. Géranton, M. Gibertini, D. Gresch, C. Johnson, T. Koretsune, *et al.*, Wannier90 as a community code: new features and applications, *Journal of Physics: Condensed Matter* **32**, 165902 (2020).
 - [144] Q. Sun, T. C. Berkelbach, J. D. McClain, and G. K.-L. Chan, Gaussian and plane-wave mixed density fitting for periodic systems, *The Journal of Chemical Physics* **147**, 164119 (2017).
 - [145] H.-Z. Ye and T. C. Berkelbach, Fast periodic gaussian density fitting by range separation, *The Journal of Chemical Physics* **154**, 131104 (2021).
 - [146] J. Haegeman, *Tensorkit* (2023).
 - [147] M. Van Damme, L. Devos, and J. Haegeman, *MPSKit* (2024).

Appendix A: Geometry trans-polyacetylene

We have optimized the structure of trans-polyacetylene (tPA) in different ways using the Vienna Ab Initio Simulation Package (VASP) [137, 138]. The structures studied in the main text, tPA1 and tPA2, have been obtained with the PBE functional [99] and with the B3LYP functional [21] on a $15 \times 1 \times 1$ k -mesh, respectively. In Fig. 8, the total final energy is plotted as a function of lattice parameter a along the chain. This scanning over a allowed to fix the shape of the unit cell for each separate run and keep the vacuum in the y and z directions constant at 20 Å.

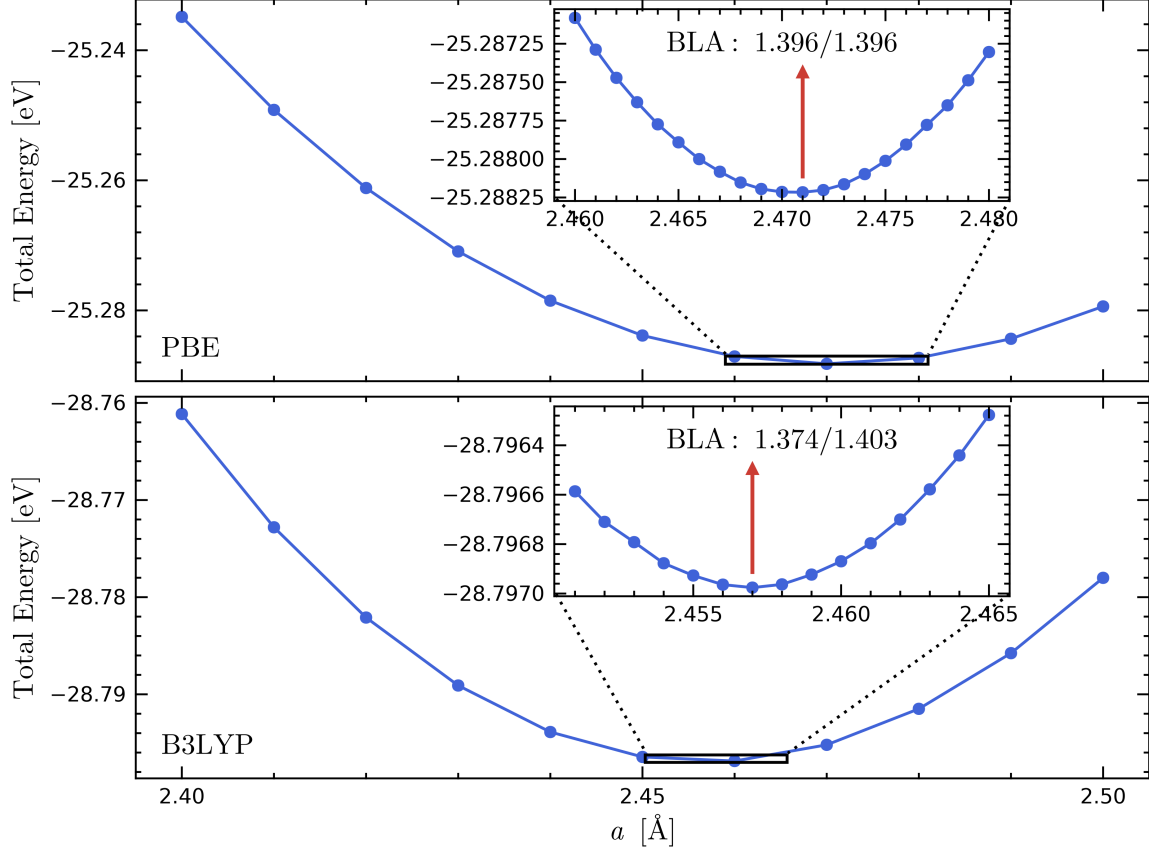


FIG. 8. The total groundstate energy of tPA after optimization with the PBE functional (top) and with the B3LYP functional (bottom) on a $15 \times 1 \times 1$ mesh, as a function of the width of the unit cell along the chain.

Appendix B: Convergence of Hubbard parameters

We show the behavior of some of the most relevant Hubbard parameters as a function of the number of k -points. For tPA, we also investigated the influence of different basis sets, namely the correlation consistent polarized valence single-zeta (cc-pVDZ) and triple-zeta (cc-pVTZ) basis sets [141].

1. Trans-polyacetylene

The convergence as a function of k -points for some of the most relevant parameters of the Hubbard model of tPA is shown in Fig. 9. For the direct interactions, $a/k + b$ fits are made to extrapolate to infinite k . These fits exclude the first three data points ($k \leq 10$). The relative difference induced by employing the larger cc-pVTZ basis set is small. The most notable relative shift occurs for $\tilde{U}_{00}^{12} = U_{0000}^{1222}$.

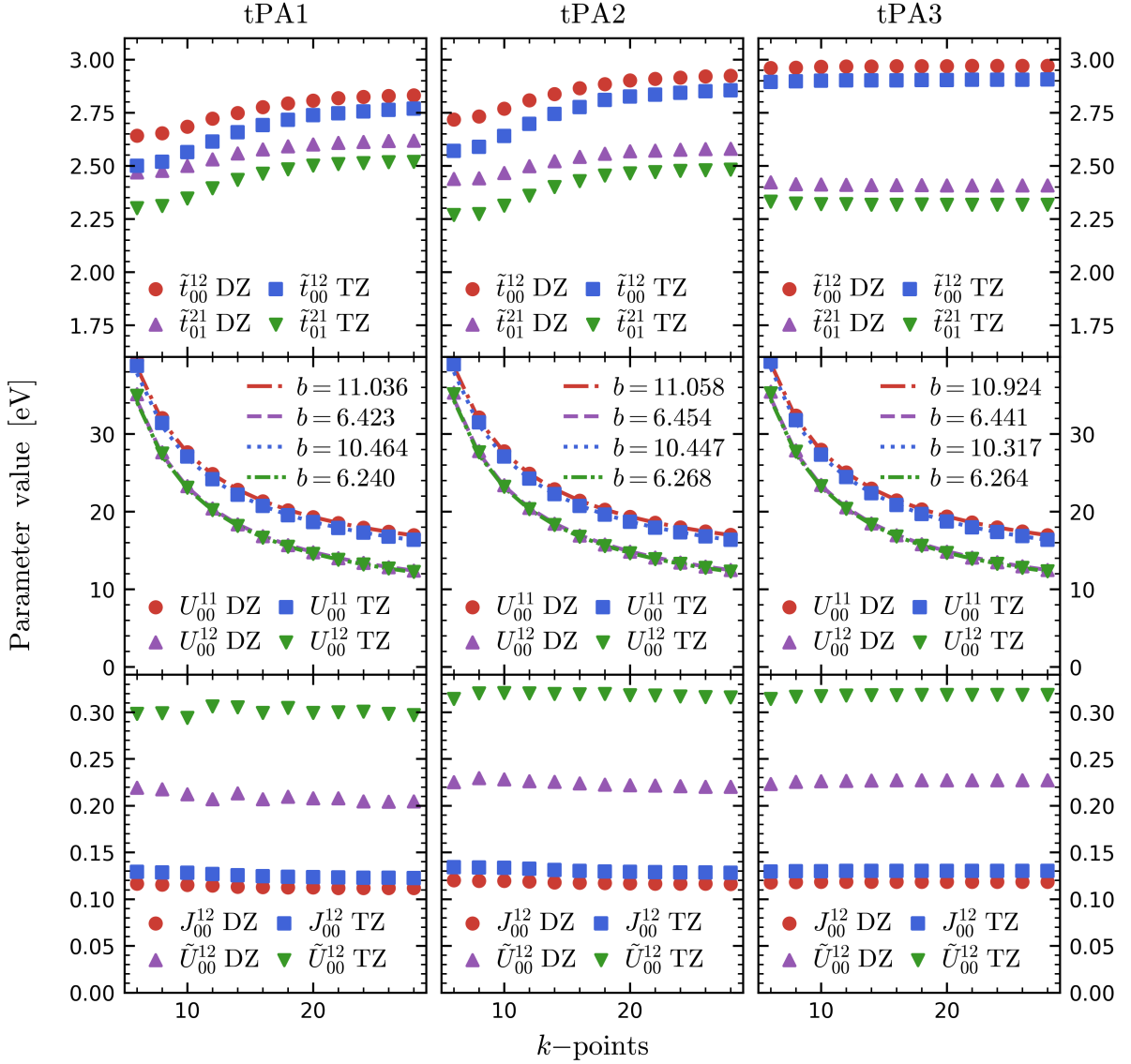


FIG. 9. The on-site interaction and nearest-neighbor tight-binding parameters in the effective Hubbard model of tPA as a function of the number of k -points along the chain. Results obtained with the cc-pVDZ (DZ) and cc-pVTZ (TZ) basis sets are given. The left, middle, and right columns correspond to the geometries tPA1, tPA2, and tPA3, respectively. For the direct interaction parameters, fits of the form $a/k + b$ are also shown, excluding the first three points ($k \leq 10$).

2. Polythiophene

The convergence as a function of k -points for some relevant parameters of the Hubbard model of polythiophene (PT) is shown in Fig. 10. For the direct interactions, $a/k + b$ fits are made to extrapolate to infinite k . These fits exclude the first three data points ($k \leq 5$). Some of the exchange and \tilde{U} parameters are not entirely converged at $k = 12$, but these are not considered in the effective model.

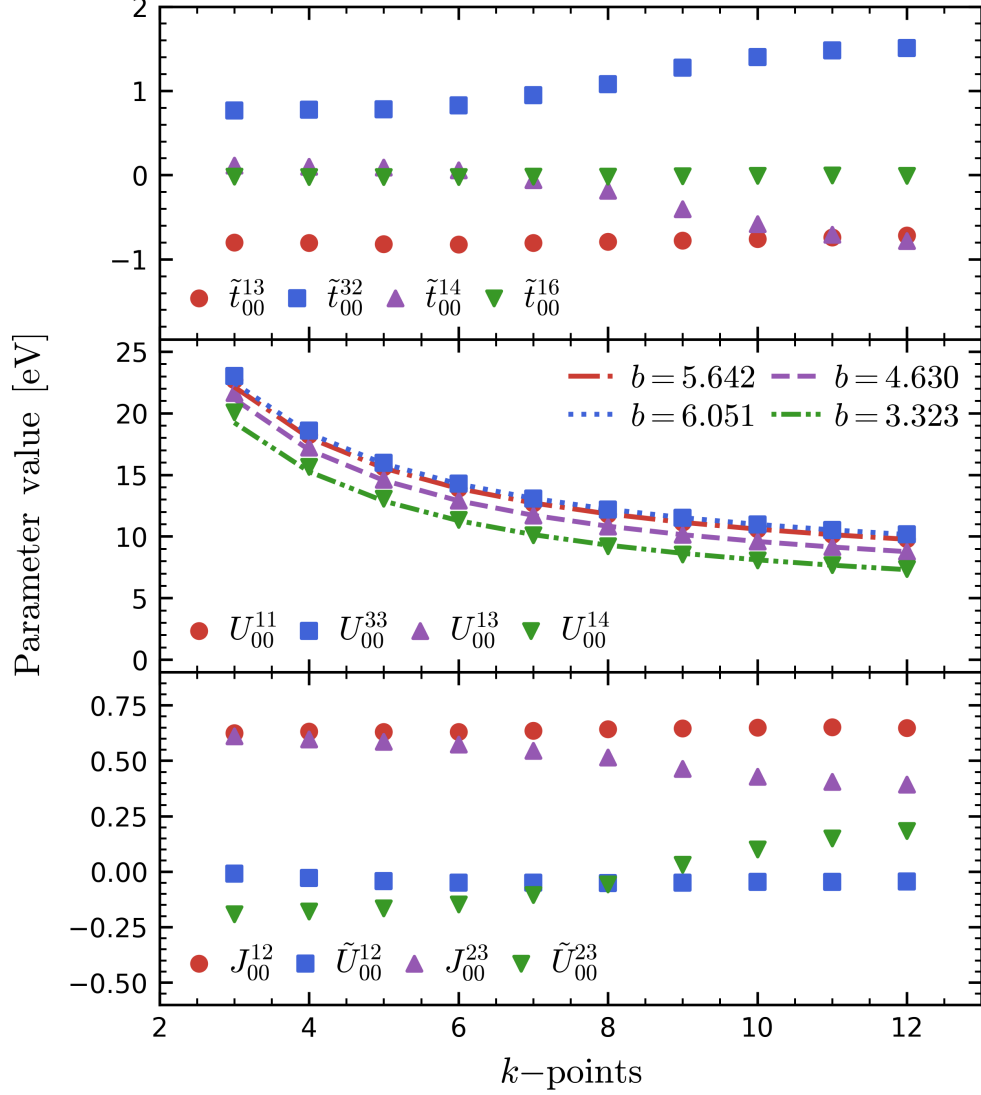


FIG. 10. Selected on-site interaction and tight-binding parameters in the effective Hubbard model of PT as a function of the number of k -points along the chain. Calculations were performed using the GTH-DZVP basis set. For direct interaction parameters, fits of the form $a/k + b$ are also shown, excluding the first three points ($k \leq 5$).

3. Sr_2CuO_3

As can be seen in Fig. 11, the parameters of the Sr_2CuO_3 Hubbard model converge fast as a function of the k -grid. To reduce computational cost, the convergence tests used slightly fewer bands (160) for the constrained random phase approximation compared to the main text calculation (192 bands).

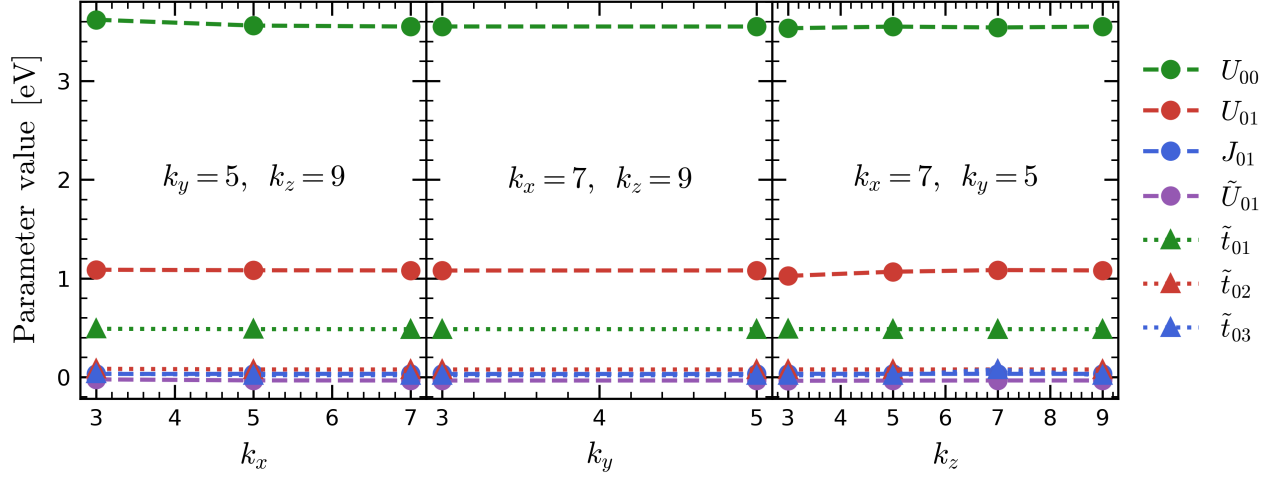


FIG. 11. The interaction and tight-binding parameters in the effective Hubbard model of Sr_2CuO_3 as a function of the number of k -points along the x , y , and z axes. The number of k -points in the corresponding perpendicular directions are set to their maximal value. An orthorhombic supercell containing four times the structure formula has been used.

Appendix C: Parameters trans-polyacetylene

We report the parameters included in the effective models for the three geometries of tPA.

1. tPA1

TABLE VI. Hopping parameters $t_{ij}^{\alpha\beta}$ included in the Hubbard model for tPA1. The elements (in eV) correspond to the parameter between band α on site $\mathbf{R}_i = [0, 0, 0]$ (rows) and band β on different sites $\mathbf{R}_j = [j, 0, 0]$ (columns).

t							
[0,0,0]		[1,0,0]		[2,0,0]		[3,0,0]	
0.587	3.552	-0.581	0.306	-0.028	-0.018	0.028	-
3.552	0.000	3.268	-0.533	0.015	-0.018	-0.020	0.027

TABLE VII: Interaction parameters (in eV) included in the Hubbard model for tPA1.

$(2i + \alpha)$	$(2j + \beta)$	$(2k + \gamma)$	$(2l + \delta)$	$U_{ijkl}^{\alpha\beta\gamma\delta}$	$(2i + \alpha)$	$(2j + \beta)$	$(2k + \gamma)$	$(2l + \delta)$	$U_{ijkl}^{\alpha\beta\gamma\delta}$
1	1	1	1	10.464	1	1	1	2	0.300
1	1	2	1	0.300	1	1	2	2	6.240
1	2	1	1	0.300	1	2	1	2	0.123
1	2	2	1	0.123	1	2	2	2	0.297
2	1	1	1	0.300	2	1	1	2	0.123
2	1	2	1	0.123	2	1	2	2	0.297
2	2	1	1	6.240	2	2	1	2	0.297
2	2	2	1	0.297	2	2	2	2	10.459
1	1	1	3	-0.251	1	1	1	4	0.085
1	1	2	3	0.054	1	2	1	3	-0.019
2	1	1	3	-0.019	2	2	1	3	-0.128
2	2	2	3	0.287	2	2	2	4	0.013
1	1	1	5	-0.034	1	1	2	5	0.043
2	2	1	5	0.027	2	2	2	5	0.073
2	2	2	6	-0.048	1	1	3	1	-0.251
1	1	3	2	0.054	1	1	4	1	0.085
1	2	3	1	-0.019	2	1	3	1	-0.019
2	2	3	1	-0.128	2	2	3	2	0.287
2	2	4	2	0.013	1	1	3	3	4.401
1	1	3	4	-0.011	1	1	4	3	-0.011
1	1	4	4	3.049	1	2	3	3	0.066
1	2	4	4	-0.013	2	1	3	3	0.066
2	1	4	4	-0.013	2	2	3	3	6.246
2	2	3	4	0.067	2	2	4	3	0.067
2	2	4	4	4.380	1	1	3	5	-0.060
2	2	3	5	-0.132	2	2	3	6	0.045
2	2	4	6	0.031	1	1	5	1	-0.034
1	1	5	2	0.043	2	2	5	1	0.027
2	2	5	2	0.073	2	2	6	2	-0.048
1	1	5	3	-0.060	2	2	5	3	-0.132
2	2	6	3	0.045	2	2	6	4	0.031
1	1	5	5	2.263	2	2	5	5	3.054
2	2	6	6	2.269	1	3	1	1	-0.251
1	3	1	2	-0.019	1	3	2	1	-0.019
1	3	2	2	-0.128	1	4	1	1	0.085
2	3	1	1	0.054	2	3	2	2	0.287
2	4	2	2	0.013	1	3	1	3	0.024
2	3	2	3	0.124	2	4	2	4	0.025
1	3	3	1	0.024	2	3	3	2	0.124
2	4	4	2	0.025	1	3	3	3	0.013

1	4	4	4	0.084	2	3	3	3	0.286
2	3	4	4	0.053	2	4	3	3	-0.130
2	4	3	4	-0.019	2	4	4	3	-0.019
2	4	4	4	-0.253	2	3	3	5	-0.020
2	4	4	5	-0.020	2	3	5	3	-0.020
2	4	5	4	-0.020	1	3	5	5	0.031
1	4	5	5	0.044	2	4	5	5	-0.134
2	4	6	6	-0.060	1	5	1	1	-0.034
1	5	2	2	0.027	2	5	1	1	0.043
2	5	2	2	0.073	2	6	2	2	-0.048
1	5	3	3	0.036	1	5	4	4	0.021
2	5	3	3	-0.026	2	5	4	4	-0.027
2	6	3	3	0.021	2	6	4	4	0.037
1	5	5	5	-0.048	2	5	5	5	0.073
2	5	6	6	0.042	2	6	5	5	0.028
2	6	6	6	-0.033	3	1	1	1	-0.251
3	1	1	2	-0.019	3	1	2	1	-0.019
3	1	2	2	-0.128	3	2	1	1	0.054
3	2	2	2	0.287	4	1	1	1	0.085
4	2	2	2	0.013	3	1	1	3	0.024
3	2	2	3	0.124	4	2	2	4	0.025
3	1	3	1	0.024	3	2	3	2	0.124
4	2	4	2	0.025	3	1	3	3	0.013
3	2	3	3	0.286	3	2	4	4	0.053
4	1	4	4	0.084	4	2	3	3	-0.130
4	2	3	4	-0.019	4	2	4	3	-0.019
4	2	4	4	-0.253	3	2	3	5	-0.020
4	2	4	5	-0.020	3	2	5	3	-0.020
4	2	5	4	-0.020	3	1	5	5	0.031
4	1	5	5	0.044	4	2	5	5	-0.134
4	2	6	6	-0.060	3	3	1	1	4.401
3	3	1	2	0.066	3	3	2	1	0.066
3	3	2	2	6.246	3	4	1	1	-0.011
3	4	2	2	0.067	4	3	1	1	-0.011
4	3	2	2	0.067	4	4	1	1	3.049
4	4	1	2	-0.013	4	4	2	1	-0.013
4	4	2	2	4.380	3	3	1	3	0.013
3	3	2	3	0.286	3	3	2	4	-0.130
3	4	2	4	-0.019	4	3	2	4	-0.019
4	4	1	4	0.084	4	4	2	3	0.053
4	4	2	4	-0.253	3	3	1	5	0.036
3	3	2	5	-0.026	3	3	2	6	0.021
4	4	1	5	0.021	4	4	2	5	-0.027
4	4	2	6	0.037	3	3	3	1	0.013
3	3	3	2	0.286	3	3	4	2	-0.130
3	4	4	2	-0.019	4	3	4	2	-0.019
4	4	3	2	0.053	4	4	4	1	0.084
4	4	4	2	-0.253	3	3	5	1	0.036
3	3	5	2	-0.026	3	3	6	2	0.021
4	4	5	1	0.021	4	4	5	2	-0.027
4	4	6	2	0.037	3	5	1	1	-0.060
3	5	2	2	-0.132	3	6	2	2	0.045
4	6	2	2	0.031	3	5	2	3	-0.020
4	5	2	4	-0.020	3	5	3	2	-0.020
4	5	4	2	-0.020	5	1	1	1	-0.034
5	1	2	2	0.027	5	2	1	1	0.043
5	2	2	2	0.073	6	2	2	2	-0.048
5	1	3	3	0.036	5	1	4	4	0.021
5	2	3	3	-0.026	5	2	4	4	-0.027
6	2	3	3	0.021	6	2	4	4	0.037
5	1	5	5	-0.048	5	2	5	5	0.073
5	2	6	6	0.042	6	2	5	5	0.028
6	2	6	6	-0.033	5	3	1	1	-0.060
5	3	2	2	-0.132	6	3	2	2	0.045

6	4	2	2	0.031	5	3	2	3	-0.020
5	4	2	4	-0.020	5	3	3	2	-0.020
5	4	4	2	-0.020	5	5	1	1	2.263
5	5	2	2	3.054	6	6	2	2	2.269
5	5	1	3	0.031	5	5	1	4	0.044
5	5	2	4	-0.134	6	6	2	4	-0.060
5	5	1	5	-0.048	5	5	2	5	0.073
5	5	2	6	0.028	6	6	2	5	0.042
6	6	2	6	-0.033	5	5	3	1	0.031
5	5	4	1	0.044	5	5	4	2	-0.134
6	6	4	2	-0.060	5	5	5	1	-0.048
5	5	5	2	0.073	5	5	6	2	0.028
6	6	5	2	0.042	6	6	6	2	-0.033

2. tPA2

TABLE VIII. Hopping parameters $t_{ij}^{\alpha\beta}$ included in the Hubbard model for tPA2. The elements (in eV) correspond to the parameter between band α on site $\mathbf{R}_i = [0, 0, 0]$ (rows) and band β on different sites $\mathbf{R}_j = [j, 0, 0]$ (columns).

t							
[0,0,0]		[1,0,0]		[2,0,0]		[3,0,0]	
0.000	3.712	-0.593	0.316	-0.020	-0.025	0.032	-
3.712	0.000	3.220	-0.546	0.017	-0.020	-0.022	0.029

TABLE IX: Interaction parameters (in eV) included in the Hubbard model for tPA2.

$(2i + \alpha)$	$(2j + \beta)$	$(2k + \gamma)$	$(2l + \delta)$	$U_{ijkl}^{\alpha\beta\gamma\delta}$	$(2i + \alpha)$	$(2j + \beta)$	$(2k + \gamma)$	$(2l + \delta)$	$U_{ijkl}^{\alpha\beta\gamma\delta}$
1	1	1	1	10.447	1	1	1	2	0.316
1	1	2	1	0.316	1	1	2	2	6.268
1	2	1	1	0.316	1	2	1	2	0.128
1	2	2	1	0.128	1	2	2	2	0.316
2	1	1	1	0.316	2	1	1	2	0.128
2	1	2	1	0.128	2	1	2	2	0.316
2	2	1	1	6.269	2	2	1	2	0.316
2	2	2	1	0.316	2	2	2	2	10.447
1	1	1	3	-0.256	1	1	1	4	0.088
1	1	2	3	0.055	1	2	1	3	-0.020
2	1	1	3	-0.020	2	2	1	3	-0.131
2	2	2	3	0.287	1	1	1	5	-0.033
1	1	2	5	0.043	1	2	2	5	0.010
2	1	2	5	0.010	2	2	1	5	0.029
2	2	2	5	0.074	2	2	2	6	-0.049
1	1	3	1	-0.256	1	1	3	2	0.055
1	1	4	1	0.088	1	2	3	1	-0.020
2	1	3	1	-0.020	2	2	3	1	-0.131
2	2	3	2	0.287	1	1	3	3	4.409
1	1	3	4	-0.011	1	1	4	3	-0.011
1	1	4	4	3.065	1	2	3	3	0.072
1	2	4	4	-0.011	2	1	3	3	0.072
2	1	4	4	-0.011	2	2	3	3	6.240
2	2	3	4	0.072	2	2	4	3	0.072
2	2	4	4	4.409	1	1	3	5	-0.061
2	2	3	5	-0.135	2	2	3	6	0.046
2	2	4	6	0.030	1	1	5	1	-0.033
1	1	5	2	0.043	1	2	5	2	0.010
2	1	5	2	0.010	2	2	5	1	0.029

2	2	5	2	0.074	2	2	6	2	-0.049
1	1	5	3	-0.061	2	2	5	3	-0.135
2	2	6	3	0.046	2	2	6	4	0.030
1	1	5	5	2.278	2	2	5	5	3.067
2	2	6	6	2.278	1	3	1	1	-0.256
1	3	1	2	-0.020	1	3	2	1	-0.020
1	3	2	2	-0.131	1	4	1	1	0.088
2	3	1	1	0.055	2	3	2	2	0.287
1	3	1	3	0.025	2	3	2	3	0.123
2	4	2	4	0.025	1	3	3	1	0.025
2	3	3	2	0.123	2	4	4	2	0.025
1	4	4	4	0.088	2	3	3	3	0.287
2	3	4	4	0.055	2	4	3	3	-0.131
2	4	3	4	-0.020	2	4	4	3	-0.020
2	4	4	4	-0.256	2	3	3	5	-0.020
2	4	4	5	-0.020	2	3	5	3	-0.020
2	4	5	4	-0.020	1	3	5	5	0.030
1	4	5	5	0.046	2	4	5	5	-0.135
2	4	6	6	-0.061	1	5	1	1	-0.033
1	5	2	2	0.029	2	5	1	1	0.043
2	5	1	2	0.010	2	5	2	1	0.010
2	5	2	2	0.074	2	6	2	2	-0.049
1	5	3	3	0.039	1	5	4	4	0.023
2	5	3	3	-0.029	2	5	4	4	-0.029
2	6	3	3	0.023	2	6	4	4	0.039
1	5	5	5	-0.049	2	5	5	5	0.074
2	5	5	6	0.010	2	5	6	5	0.010
2	5	6	6	0.043	2	6	5	5	0.029
2	6	6	6	-0.033	3	1	1	1	-0.256
3	1	1	2	-0.020	3	1	2	1	-0.020
3	1	2	2	-0.131	3	2	1	1	0.055
3	2	2	2	0.287	4	1	1	1	0.088
3	1	1	3	0.025	3	2	2	3	0.123
4	2	2	4	0.025	3	1	3	1	0.025
3	2	3	2	0.123	4	2	4	2	0.025
3	2	3	3	0.287	3	2	4	4	0.055
4	1	4	4	0.088	4	2	3	3	-0.131
4	2	3	4	-0.020	4	2	4	3	-0.020
4	2	4	4	-0.256	3	2	3	5	-0.020
4	2	4	5	-0.020	3	2	5	3	-0.020
4	2	5	4	-0.020	3	1	5	5	0.030
4	1	5	5	0.046	4	2	5	5	-0.135
4	2	6	6	-0.061	3	3	1	1	4.409
3	3	1	2	0.072	3	3	2	1	0.072
3	3	2	2	6.240	3	4	1	1	-0.011
3	4	2	2	0.072	4	3	1	1	-0.011
4	3	2	2	0.072	4	4	1	1	3.065
4	4	1	2	-0.011	4	4	2	1	-0.011
4	4	2	2	4.409	3	3	2	3	0.287
3	3	2	4	-0.131	3	4	2	4	-0.020
4	3	2	4	-0.020	4	4	1	4	0.088
4	4	2	3	0.055	4	4	2	4	-0.256
3	3	1	5	0.039	3	3	2	5	-0.029
3	3	2	6	0.023	4	4	1	5	0.023
4	4	2	5	-0.029	4	4	2	6	0.039
3	3	3	2	0.287	3	3	4	2	-0.131
3	4	4	2	-0.020	4	3	4	2	-0.020
4	4	3	2	0.055	4	4	4	1	0.088
4	4	4	2	-0.256	3	3	5	1	0.039
3	3	5	2	-0.029	3	3	6	2	0.023
4	4	5	1	0.023	4	4	5	2	-0.029
4	4	6	2	0.039	3	5	1	1	-0.061
3	5	2	2	-0.135	3	6	2	2	0.046
4	6	2	2	0.030	3	5	2	3	-0.020

4	5	2	4	-0.020	3	5	3	2	-0.020
4	5	4	2	-0.020	5	1	1	1	-0.033
5	1	2	2	0.029	5	2	1	1	0.043
5	2	1	2	0.010	5	2	2	1	0.010
5	2	2	2	0.074	6	2	2	2	-0.049
5	1	3	3	0.039	5	1	4	4	0.023
5	2	3	3	-0.029	5	2	4	4	-0.029
6	2	3	3	0.023	6	2	4	4	0.039
5	1	5	5	-0.049	5	2	5	5	0.074
5	2	5	6	0.010	5	2	6	5	0.010
5	2	6	6	0.043	6	2	5	5	0.029
6	2	6	6	-0.033	5	3	1	1	-0.061
5	3	2	2	-0.135	6	3	2	2	0.046
6	4	2	2	0.030	5	3	2	3	-0.020
5	4	2	4	-0.020	5	3	3	2	-0.020
5	4	4	2	-0.020	5	5	1	1	2.278
5	5	2	2	3.067	6	6	2	2	2.278
5	5	1	3	0.030	5	5	1	4	0.046
5	5	2	4	-0.135	6	6	2	4	-0.061
5	5	1	5	-0.049	5	5	2	5	0.074
5	5	2	6	0.029	5	6	2	5	0.010
6	5	2	5	0.010	6	6	2	5	0.043
6	6	2	6	-0.033	5	5	3	1	0.030
5	5	4	1	0.046	5	5	4	2	-0.135
6	6	4	2	-0.061	5	5	5	1	-0.049
5	5	5	2	0.074	5	5	6	2	0.029
5	6	5	2	0.010	6	5	5	2	0.010
6	6	5	2	0.043	6	6	6	2	-0.033

3. tPA3

TABLE X. Hopping parameters $t_{ij}^{\alpha\beta}$ included in the Hubbard model for tPA3. The elements (in eV) correspond to the parameter between band α on site $\mathbf{R}_i = [0, 0, 0]$ (rows) and band β on different sites $\mathbf{R}_j = [j, 0, 0]$ (columns).

t							
[0,0,0]		[1,0,0]		[2,0,0]		[3,0,0]	
0.000	3.803	-0.548	0.298	-0.010	-0.034	0.031	-
3.803	0.000	2.977	-0.501	0.005	-0.010	-0.022	0.029

TABLE XI: Interaction parameters (in eV) included in the Hubbard model for tPA3.

$(2i + \alpha)$	$(2j + \beta)$	$(2k + \gamma)$	$(2l + \delta)$	$U_{ijkl}^{\alpha\beta\gamma\delta}$	$(2i + \alpha)$	$(2j + \beta)$	$(2k + \gamma)$	$(2l + \delta)$	$U_{ijkl}^{\alpha\beta\gamma\delta}$
1	1	1	1	10.317	1	1	1	2	0.318
1	1	2	1	0.318	1	1	2	2	6.264
1	2	1	1	0.318	1	2	1	2	0.130
1	2	2	1	0.130	1	2	2	2	0.318
2	1	1	1	0.318	2	1	1	2	0.130
2	1	2	1	0.130	2	1	2	2	0.318
2	2	1	1	6.264	2	2	1	2	0.318
2	2	2	1	0.318	2	2	2	2	10.317
1	1	1	3	-0.250	1	1	1	4	0.087
1	1	2	3	0.053	1	2	1	3	-0.019
2	1	1	3	-0.019	2	2	1	3	-0.123
2	2	1	4	-0.013	2	2	2	3	0.259
2	2	2	4	0.014	1	1	1	5	-0.028
1	1	2	5	0.041	2	2	1	5	0.030

2	2	2	5	0.069	2	2	2	6	-0.048
1	1	3	1	-0.250	1	1	3	2	0.053
1	1	4	1	0.087	1	2	3	1	-0.019
2	1	3	1	-0.019	2	2	3	1	-0.123
2	2	3	2	0.259	2	2	4	1	-0.013
2	2	4	2	0.014	1	1	3	3	4.407
1	1	3	4	-0.010	1	1	4	3	-0.010
1	1	4	4	3.075	1	2	3	3	0.075
1	2	4	4	-0.010	2	1	3	3	0.075
2	1	4	4	-0.010	2	2	3	3	6.162
2	2	3	4	0.075	2	2	4	3	0.075
2	2	4	4	4.407	1	1	3	5	-0.062
2	2	3	5	-0.133	2	2	3	6	0.046
2	2	4	6	0.029	1	1	5	1	-0.028
1	1	5	2	0.041	2	2	5	1	0.030
2	2	5	2	0.069	2	2	6	2	-0.048
1	1	5	3	-0.062	2	2	5	3	-0.133
2	2	6	3	0.046	2	2	6	4	0.029
1	1	5	5	2.284	2	2	5	5	3.065
2	2	6	6	2.284	1	3	1	1	-0.250
1	3	1	2	-0.019	1	3	2	1	-0.019
1	3	2	2	-0.123	1	4	1	1	0.087
1	4	2	2	-0.013	2	3	1	1	0.053
2	3	2	2	0.259	2	4	2	2	0.014
1	3	1	3	0.025	2	3	2	3	0.113
2	4	2	4	0.025	1	3	3	1	0.025
2	3	3	2	0.113	2	4	4	2	0.025
1	3	3	3	0.014	1	4	3	3	-0.013
1	4	4	4	0.087	2	3	3	3	0.259
2	3	4	4	0.053	2	4	3	3	-0.123
2	4	3	4	-0.019	2	4	4	3	-0.019
2	4	4	4	-0.250	2	3	3	5	-0.019
2	4	4	5	-0.019	2	3	5	3	-0.019
2	4	5	4	-0.019	1	3	5	5	0.029
1	4	5	5	0.046	2	4	5	5	-0.133
2	4	6	6	-0.062	1	5	1	1	-0.028
1	5	2	2	0.030	2	5	1	1	0.041
2	5	2	2	0.069	2	6	2	2	-0.048
1	5	3	3	0.038	1	5	4	4	0.023
2	5	3	3	-0.033	2	5	4	4	-0.033
2	6	3	3	0.023	2	6	4	4	0.038
1	5	5	5	-0.048	2	5	5	5	0.069
2	5	6	6	0.041	2	6	5	5	0.030
2	6	6	6	-0.028	3	1	1	1	-0.250
3	1	1	2	-0.019	3	1	2	1	-0.019
3	1	2	2	-0.123	3	2	1	1	0.053
3	2	2	2	0.259	4	1	1	1	0.087
4	1	2	2	-0.013	4	2	2	2	0.014
3	1	1	3	0.025	3	2	2	3	0.113
4	2	2	4	0.025	3	1	3	1	0.025
3	2	3	2	0.113	4	2	4	2	0.025
3	1	3	3	0.014	3	2	3	3	0.259
3	2	4	4	0.053	4	1	3	3	-0.013
4	1	4	4	0.087	4	2	3	3	-0.123
4	2	3	4	-0.019	4	2	4	3	-0.019
4	2	4	4	-0.250	3	2	3	5	-0.019
4	2	4	5	-0.019	3	2	5	3	-0.019
4	2	5	4	-0.019	3	1	5	5	0.029
4	1	5	5	0.046	4	2	5	5	-0.133
4	2	6	6	-0.062	3	3	1	1	4.407
3	3	1	2	0.075	3	3	2	1	0.075
3	3	2	2	6.162	3	4	1	1	-0.010
3	4	2	2	0.075	4	3	1	1	-0.010
4	3	2	2	0.075	4	4	1	1	3.075

4	4	1	2	-0.010	4	4	2	1	-0.010
4	4	2	2	4.407	3	3	1	3	0.014
3	3	1	4	-0.013	3	3	2	3	0.259
3	3	2	4	-0.123	3	4	2	4	-0.019
4	3	2	4	-0.019	4	4	1	4	0.087
4	4	2	3	0.053	4	4	2	4	-0.250
3	3	1	5	0.038	3	3	2	5	-0.033
3	3	2	6	0.023	4	4	1	5	0.023
4	4	2	5	-0.033	4	4	2	6	0.038
3	3	3	1	0.014	3	3	3	2	0.259
3	3	4	1	-0.013	3	3	4	2	-0.123
3	4	4	2	-0.019	4	3	4	2	-0.019
4	4	3	2	0.053	4	4	4	1	0.087
4	4	4	2	-0.250	3	3	5	1	0.038
3	3	5	2	-0.033	3	3	6	2	0.023
4	4	5	1	0.023	4	4	5	2	-0.033
4	4	6	2	0.038	3	5	1	1	-0.062
3	5	2	2	-0.133	3	6	2	2	0.046
4	6	2	2	0.029	3	5	2	3	-0.019
4	5	2	4	-0.019	3	5	3	2	-0.019
4	5	4	2	-0.019	5	1	1	1	-0.028
5	1	2	2	0.030	5	2	1	1	0.041
5	2	2	2	0.069	6	2	2	2	-0.048
5	1	3	3	0.038	5	1	4	4	0.023
5	2	3	3	-0.033	5	2	4	4	-0.033
6	2	3	3	0.023	6	2	4	4	0.038
5	1	5	5	-0.048	5	2	5	5	0.069
5	2	6	6	0.041	6	2	5	5	0.030
6	2	6	6	-0.028	5	3	1	1	-0.062
5	3	2	2	-0.133	6	3	2	2	0.046
6	4	2	2	0.029	5	3	2	3	-0.019
5	4	2	4	-0.019	5	3	3	2	-0.019
5	4	4	2	-0.019	5	5	1	1	2.284
5	5	2	2	3.065	6	6	2	2	2.284
5	5	1	3	0.029	5	5	1	4	0.046
5	5	2	4	-0.133	6	6	2	4	-0.062
5	5	1	5	-0.048	5	5	2	5	0.069
5	5	2	6	0.030	6	6	2	5	0.041
6	6	2	6	-0.028	5	5	3	1	0.029
5	5	4	1	0.046	5	5	4	2	-0.133
6	6	4	2	-0.062	5	5	5	1	-0.048
5	5	5	2	0.069	5	5	6	2	0.030
6	6	5	2	0.041	6	6	6	2	-0.028

Appendix D: Convergence of band gap

We show that the reported band gap values are converged as a function of the bond dimension.

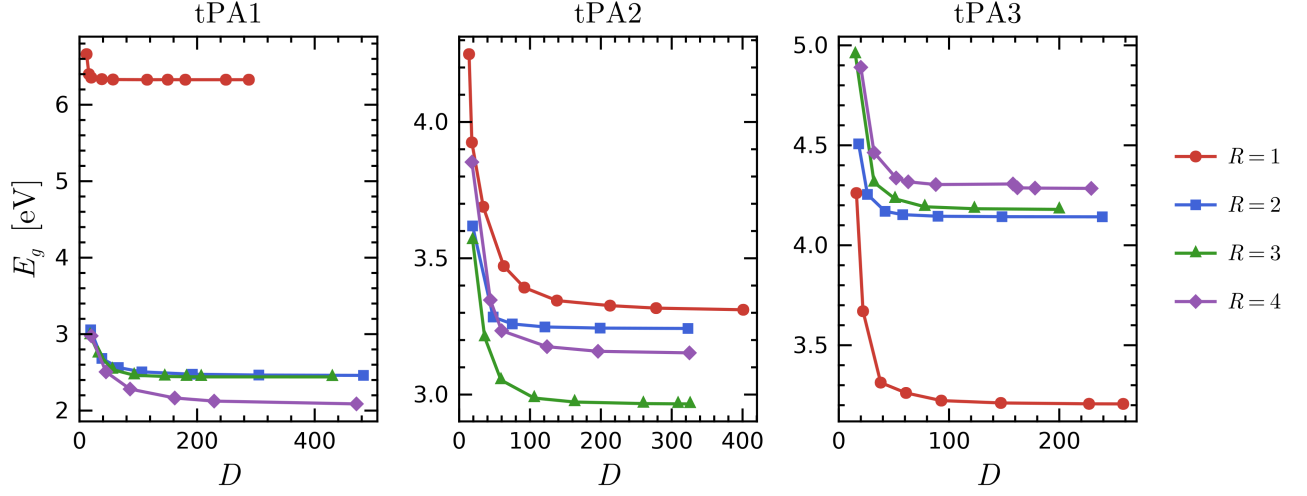


FIG. 12. The band gap of the three tPA structures for different ranges R , as a function of the maximal bond dimension in the unit cell.

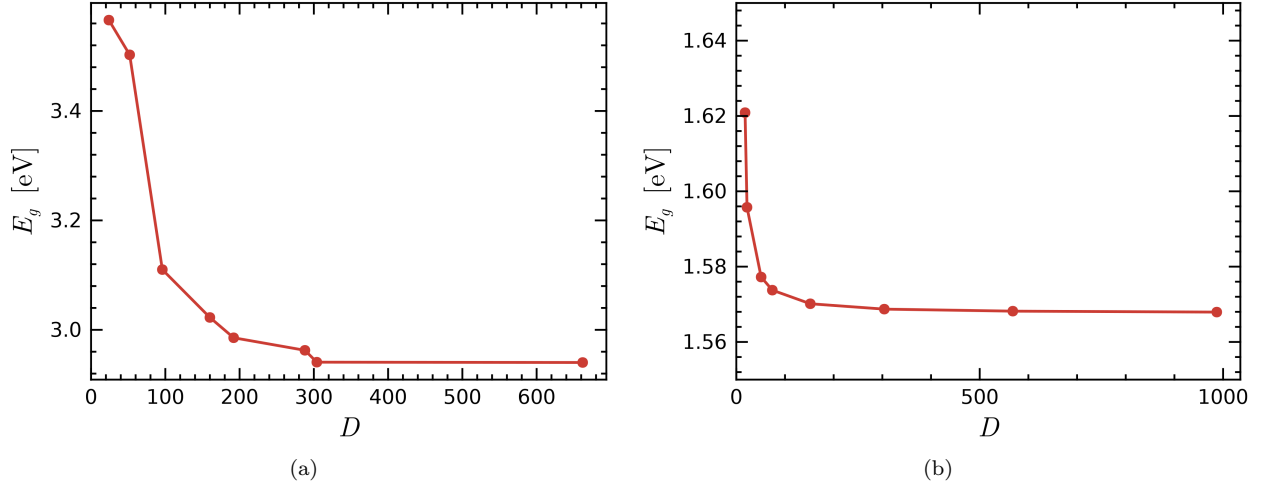


FIG. 13. The band gap of (a) PT and (b) Sr_2CuO_3 as a function of the maximal bond dimension in the unit cell.